Electronic Supplementary Material (ESI) for Journal of Materials Chemistry A.

# Unfolding the terahertz spectrum of soft porous crystals: rigid unit modes and their impact on phase transitions

Alexander E. J. Hoffman,[†] Irena Senkovska,[*‡] Jelle Wieme,[†] Alexander Krylov,[¶] Stefan Kaskel,[‡] and Veronique Van Speybroeck[*†]

†*Center for Molecular Modeling, Ghent University, Technologiepark 46, 9052 Zwijnaarde, Belgium*
‡*Inorganic Chemistry I, Technische Universität Dresden, Bergstraße 66, 01187 Dresden, Germany*
¶*Kirensky Institute of Physics, Federal Research Center KSC SB RAS, 660036, Krasnoyarsk, Russia*

**E-mail: Veronique.VanSpeybroeck@UGent.be**
**E-mail: irena.senkovska@tu-dresden.de**

## Supporting Information

# Contents

# S1 The reduced Hessian approach

In the following section, the implementation of the reduced Hessian technique will be further clarified. First, the construction of the projection matrix will be explained, followed by a mathematical proof of the orthonormality of real and reduced normal modes. The overlap of the obtained reduced normal modes and the real normal modes will also be evaluated.

## S1.1 The projection matrix

Once a subdivision in $M$ building blocks is defined, a projection matrix $P$ with dimensions $3N \times 6M$ can be constructed, with $N$ the number of atoms in the unit cell. The columns of $P$ describe translations and rotations of the building blocks in the original basis *i.e.* the cell vectors $\vec{a}$, $\vec{b}$, and $\vec{c}$. Each building block has therefore 6 different contributions to the projection matrix: 3 translations along $\vec{a}$, $\vec{b}$, and $\vec{c}$ and 3 rotations around $\vec{a}$, $\vec{b}$, and $\vec{c}$. The translation vector of building block $i$ along vector $\vec{a} = [a_1, a_2, a_3]$ has the following form:

$$T_{ia} = C * \left[ 0 \cdots 0 \; \underbrace{\underbrace{a_1 * w_1 \; a_2 * w_1 \; a_3 * w_1}_{\text{atom 1}} \cdots \underbrace{a_1 * w_n \; a_2 * w_n \; a_3 * w_n}_{\text{atom } n}}_{\text{block } i} \; 0 \cdots 0 \right] \tag{1}$$

where $w_1 \cdots w_n$ represent the weighting factor of atoms $1 \cdots n$ belonging to building block $i$ ($\frac{1}{2}$ for atom in hydroxyl group, $\frac{1}{3}$ for carbon atom in carboxyl group, 1 for other atoms). $C$ is the normalization constant to make $T_{ia}$ a unit vector. For translation along the other cell vectors, $\vec{a}$ is replaced by $\vec{b}$ or $\vec{c}$. Similarly, the rotation vector of building block $i$ along vector $\vec{a} = [a_1, a_2, a_3]$ has the following form:

$$R_{ia} = C * \left[ 0 \cdots 0 \; \underbrace{\underbrace{A_{11} * w_1 \; A_{12} * w_1 \; A_{13} * w_1}_{\text{atom 1}} \cdots \underbrace{A_{n1} * w_n \; A_{n2} * w_n \; A_{n3} * w_n}_{\text{atom } n}}_{\text{block } i} \; 0 \cdots 0 \right] \tag{2}$$

where $\vec{A_j} = [A_{j1}, A_{j2}, A_{j3}]$ is defined as:

$$\vec{A_j} = \vec{a} \times \vec{d_j} \tag{3}$$

with $\vec{d_j}$ the distance vector between atom $j$ and the center of mass of building block $i$. The other variables are identical to those appearing in the expression of the translation vector.

## S1.2 Reduced vs real normal modes

Via the projection matrix, the reduced Hessian can be constructed according to the procedure described in the main paper. The resulting reduced normal modes follow after normal mode analysis. These reduced normal modes can be expressed in the original basis after matrix multiplication with the projection matrix. In this form, they can be compared with the real normal modes obtained from the original Hessian. Both the real and the reduced normal modes are orthonormal vectors.

Figures S1 and S2 visualize the overlap (by means of the dot product) between the original normal modes and the reduced normal modes in the original basis for the lp and cp phase structures, respectively. Modes with an overlap value close to 1 are almost similar, whereas modes with an overlap value close to 0 have a completely different origin. From Figures S1

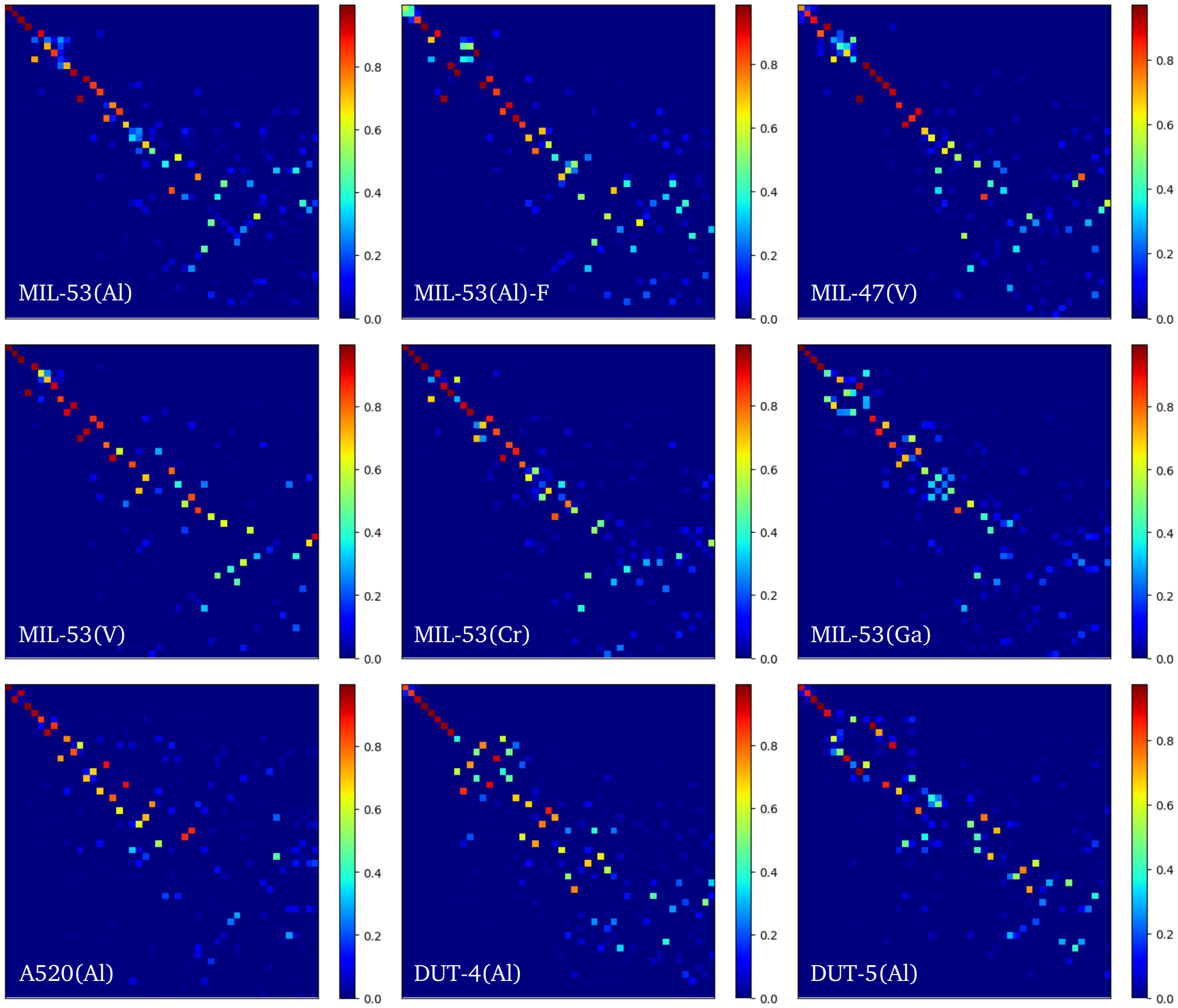

**Figure S1:** Visualization of the dot products of the reduced normal modes (vertical) with the real normal modes (horizontal) of the structures in the lp phase

and S2, it is clear that the normal modes with the lowest frequencies, *i.e.* the rigid unit modes (RUMs), are very well described by the reduced normal modes evidenced by a high overlap value. Modes with a higher frequency are less well described by building block translations and rotations alone, hence the reduced normal modes can no longer reproduce these modes and the overlap values are lower.

Even though the reduced normal modes can be used to detect equal RUMs in different structures, in some cases they are not able to connect similar normal modes correctly and they have to be connected manually. This rarely happens in the lp phase structures (see Table S1, but there are some cases in the cp phase structures (see Table S2).

**Table S1:** Normal modes that were manually linked with their counterpart in the lp phase of MIL-53(Al)

| | mode 4 | mode 8 |
|---|---|---|
| MIL-53(Ga) | | mode 10 |
| MIL-53(Al)-F | mode 4 | mode 9 |

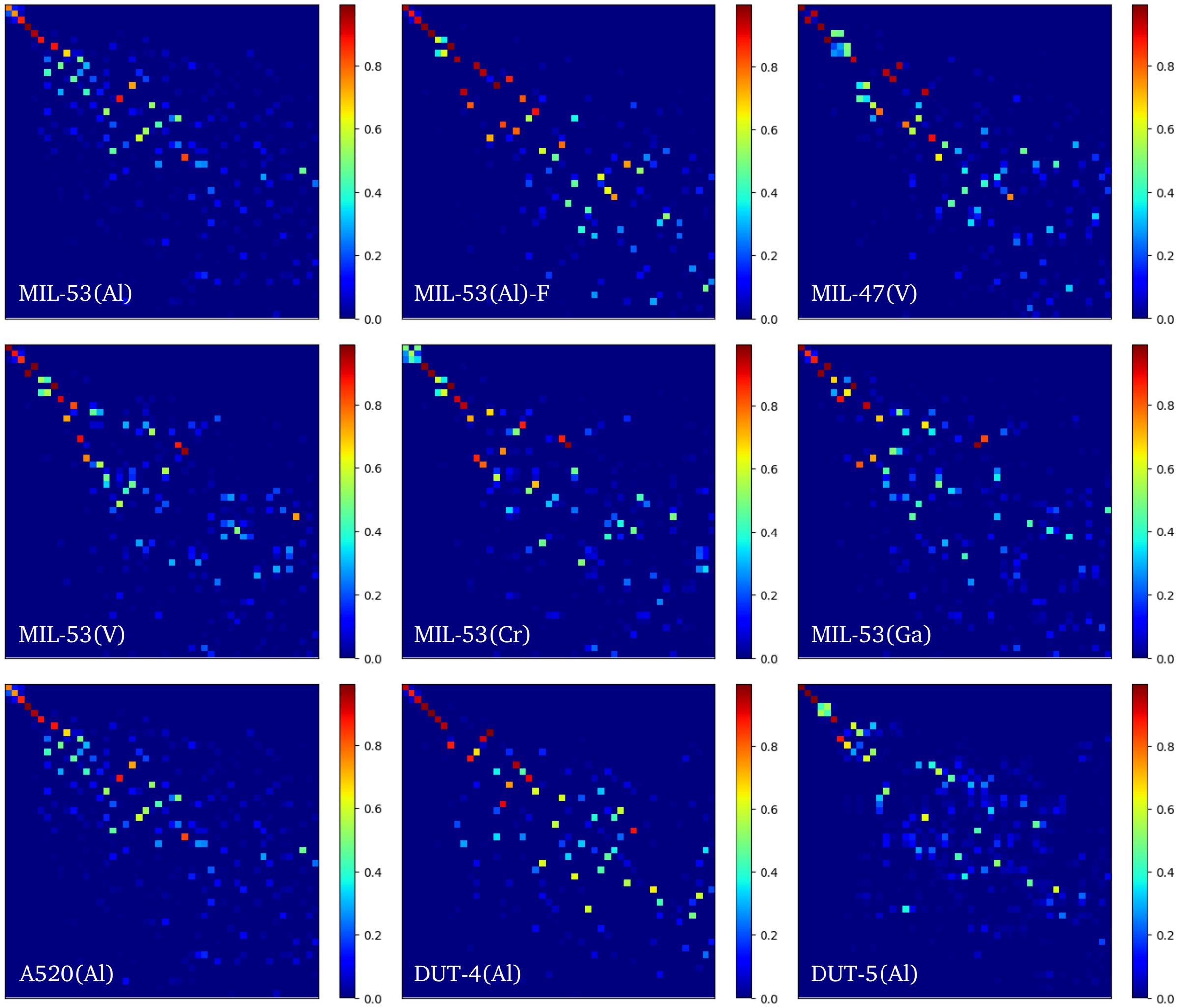

**Figure S2:** Visualization of the dot products of the reduced normal modes (vertical) with the real normal modes (horizontal) of the structures in the cp phase

**Table S2:** Normal modes that were manually linked with their counterpart in the cp phase of MIL-53(Al)

| MIL-53(Al) | mode 5 | mode 6 | mode 7 | mode 13 | mode 14 | mode 17 | mode 18 |
|---|---|---|---|---|---|---|---|
| MIL-53(Ga) | | | | mode 13 | mode 20 | | mode 17 |
| MIL-53(Cr) | | | | | mode 16 | | |
| MIL-53(V) | | | | | mode 21 | | |
| MIL-53(Al)-F | | | | | | | |
| MIL-47(V) | | mode 6 | | | | mode 21 | |
| A520(Al) | | | mode 21 | mode 11 | mode 20 | mode 15 | mode 18 |
| DUT-4(Al) | mode 5 | | mode 12 | | | | |
| DUT-5(Al) | | | | mode 13 | | mode 24 | mode 27 |

# S2 PXRD patterns

## S2.1 MIL-53(Al)

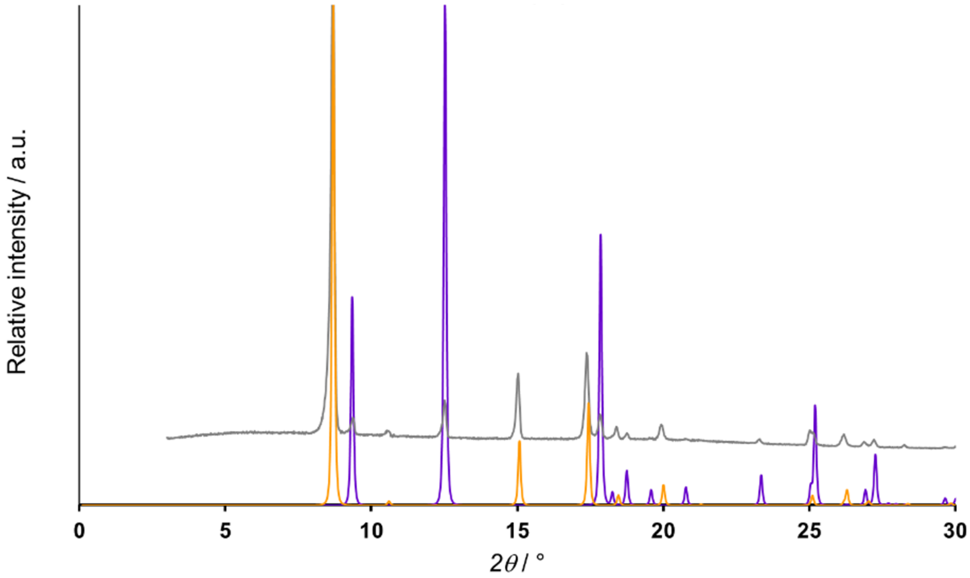

**Figure S3:** Comparison of experimental (gray) and calculated PXRD patterns of synthesized MIL-53(Al). The calculated PXRD pattern of the cp and lp phases are visualized by the purple and orange curve, respectively.

## S2.2 MIL-53(Cr)

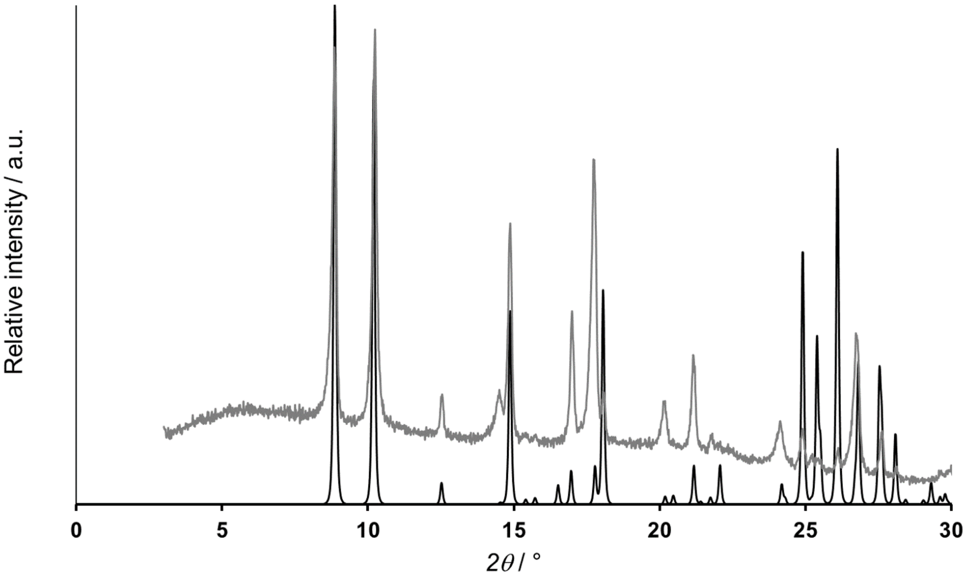

**Figure S4:** Comparison of experimental (gray) and calculated (black) PXRD patterns of synthesized MIL-53(Cr). The calculated PXRD pattern is the one of the as made sample.

## S2.3 DUT-4(Al) cp

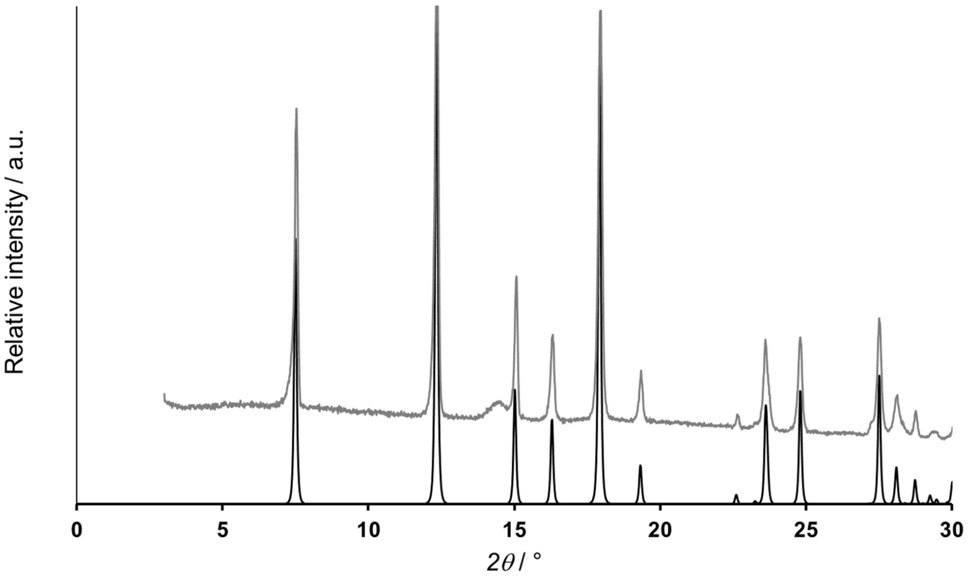

**Figure S5:** Comparison of experimental (gray) and calculated (black) PXRD patterns of synthesized DUT-4(Al) in the cp phase.

## S2.4 DUT-4(Al) lp

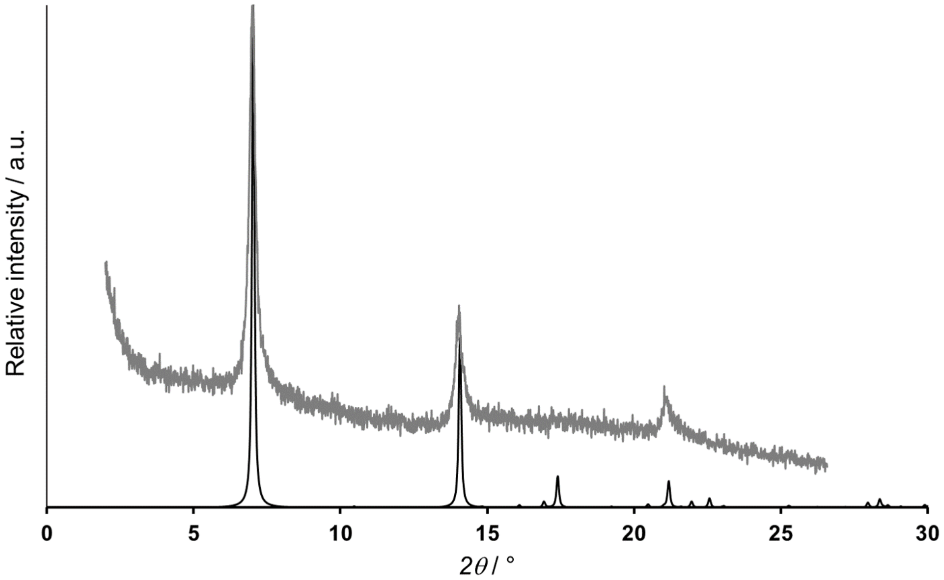

**Figure S6:** Comparison of experimental (gray) and calculated (black) PXRD patterns of synthesized DUT-4(Al) in the lp phase.

## S2.5 DUT-5(Al)

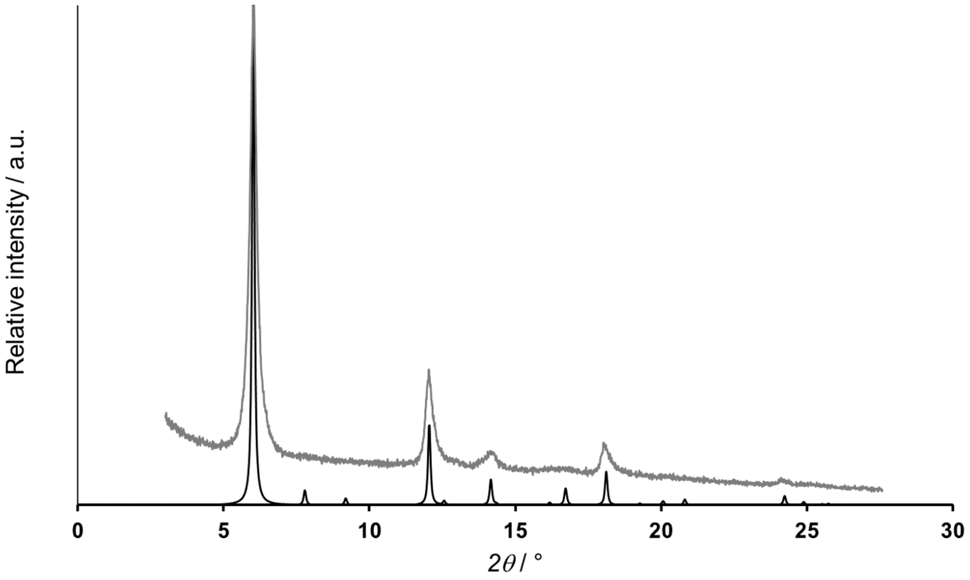

**Figure S7:** Comparison of experimental (gray) and calculated (black) PXRD patterns of synthesized DUT-5(Al) in the lp phase.

## S3 Linker alignment

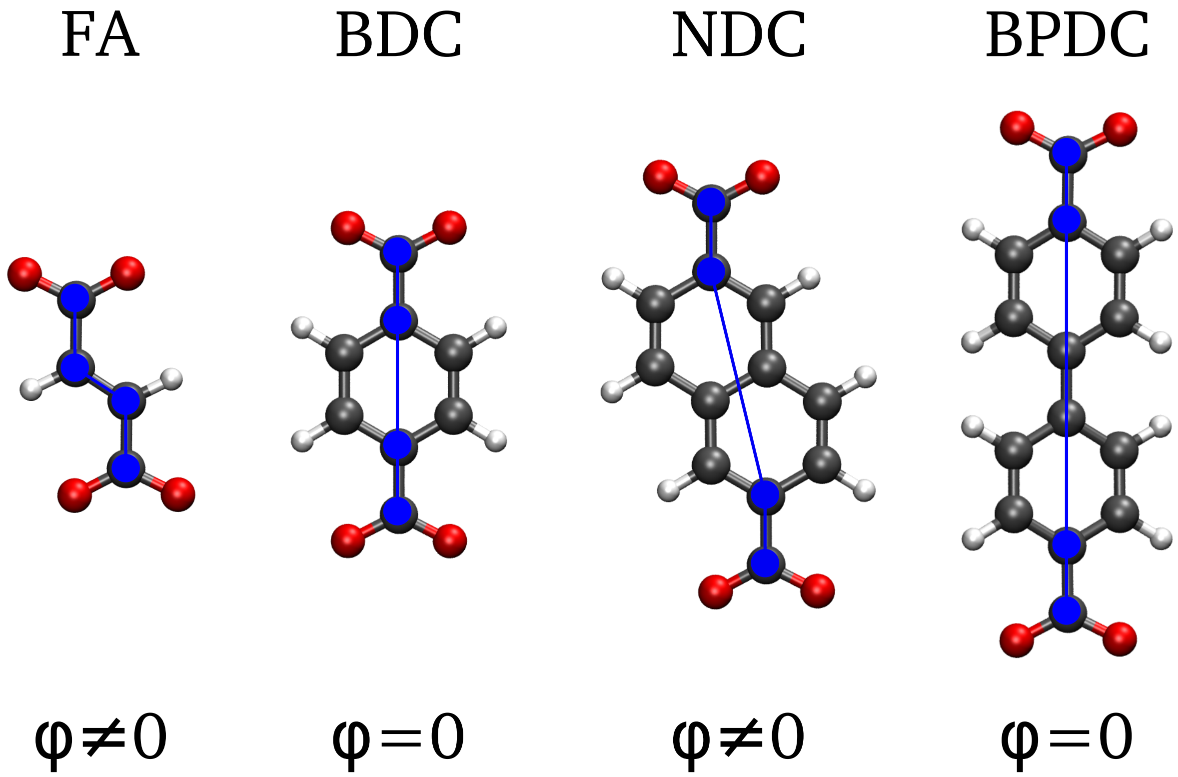

**Figure S8:** Visualization of the different types of linkers with indication of the angle between carboxyl groups, which may be aligned ($\phi = 0$) or disaligned ($\phi \neq 0$)

## S4 Effect of water on theoretical Raman spectra

The experimental Raman spectra were measured under ambient conditions, which means that residual water molecules may be adsorbed within the MOF pores. To estimate the influence of the presence of water molecules on the Raman spectra, we have explicitly determined the theoretical Raman spectrum of the hydrated np (nph) phase, which is the phase that is present under ambient conditions (see Figure S9). To account for the large mobility of the water molecules we have performed *ab initio* molecular dynamics (AIMD) simulations instead of static simulations (see section S4.1 for the computational settings). AIMD simulations on the hydrated MIL-53(Al) structure give rise to a Raman spectrum, which is in a very good agreement with the experimentally measured spectrum. Moreover, the Raman fingerprints that are observed arise mainly due to the framework vibrations. This is illustrated by comparing the AIMD result with water molecules with the static DFT Raman spectrum of MIL-53(Al) without water molecules optimized at the experimental unit cell volume. The Raman active bands almost completely overlap although some intensity differences can be observed. Clearly, the Raman spectrum of the hydrated sample is dominated by framework bands and the water molecules have only a minor contribution. Therefore, it can be considered safe to compare static DFT Raman spectra of MOFs without water molecules with experimental Raman spectra of hydrated samples.

For completeness, we have also performed AIMD simulations on the lp and cp phases without water molecules and compared them with the static results (see Figure S9). In this way, it can be verified that the phonon modes sampled by the MD simulations are those predicted by the static normal mode analysis. Dynamic Raman spectra closely resemble those obtained via static DFT calculations. This shows that the harmonic approximation can reliably predict the phonon modes in MIL-53(Al).

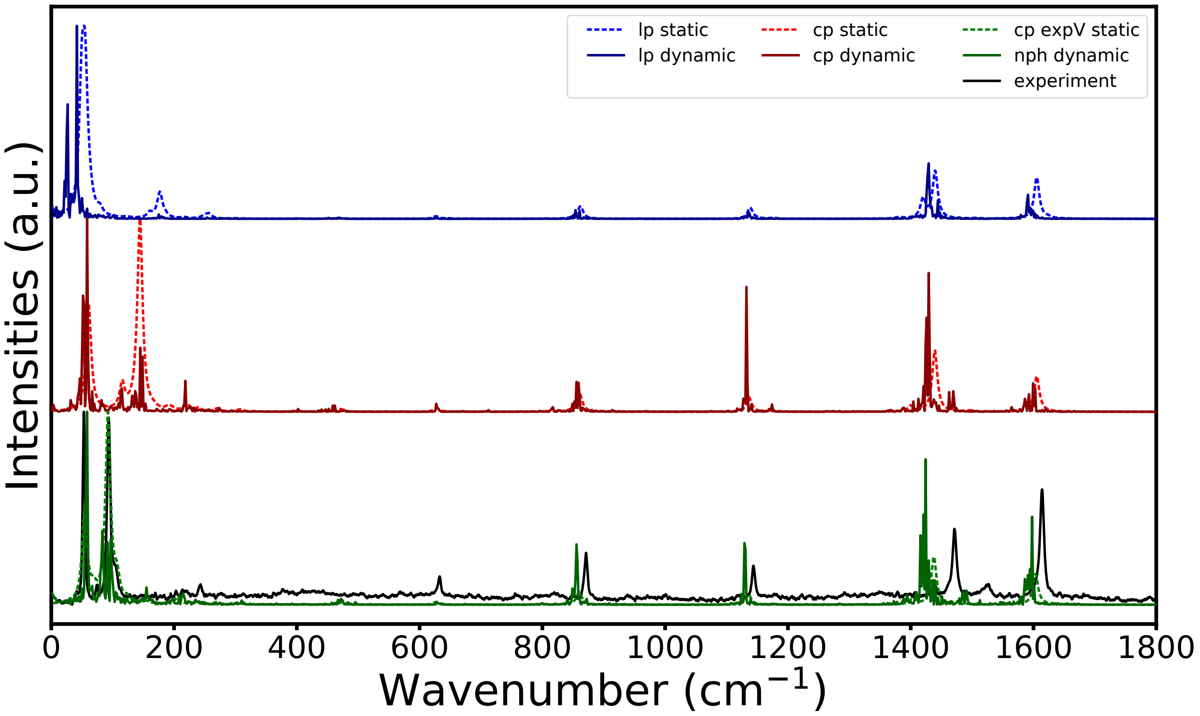

**Figure S9:** Dynamic and static Raman spectra of the lp phase (blue), cp phase (red), and the hydrated np (nph) phase (green) compared with the experimentally measured spectrum

## S4.1 Computational settings

The dynamic simulations were performed with CP2K using the Quickstep module [1] at the same level of theory as the static calculations (PBE-D3(BJ)[2, 3, 4]). The Gaussian plane wave method [5] was used with a TZVP-MOLOPT atomic basis set [6] and GTH pseudopotentials [7]. The cutoff and relative cutoff of the plane wave basis set was set to 1000 Ry and 60 Ry, respectively. All simulations were executed at the gamma point. However, the unit cell was doubled along the metal-oxide chain to accurately take into account the terahertz modes. The SCF cycle of each MD step was considered to be converged when the energy was lower than $10^{-6}$ Ha. The nph phase was first simulated in the NPT ensemble starting from the equilibrium lp phase structure with 4 water molecules per unit cell in the pores. The average cell parameters were determined and used in a subsequent simulation in the NVT ensemble. AIMD simulations of the lp and cp phase structures were only run in the NVT ensemble starting from the statically optimized structure. The temperature in the NPT and NVT simulations was fixed at 300 K using a Nosé-Hoover chain thermostat [8] with five beads and a time constant of 100 fs. The pressure in the NPT simulations was fixed at 1 bar using a Martyna Tobias Klein (MTK) barostat [9] with a time constant of 1 ps. Each simulation was initiated with an equilibration run of 5 ps followed by a production run of 20 ps with a time step of 0.5 fs. The IR and Raman spectra were predicted from the NVT simulations after calculation of, respectively, the dipole moment and polarizability tensor at subsequent time steps. The polarizability tensor was derived from the dipole moments with and without electric field by a finite difference approach [10]. Fourier transformation of (combinations of) the autocorrelation function of trajectories of dipole moments and polarizability tensors resulted in the IR and Raman spectra, respectively [10]. To ensure that the spectra were predicted in the complete IR range, dipole moments were calculated every 2 fs (every 4th MD step).

# S5 Mode characterization

## S5.1 Procedure

In this section, it will be discussed how to quantify the contribution of translations and rotations of a certain building block to a specific normal mode. In that regard, the projection matrix, consisting of translation and rotation vectors, will be of interest (see Section S1.1). We first construct a similar matrix with columns formed by mass-weighted translation and rotation vectors. This matrix with dimensions $3N \times 6M$ can be matrix multiplied with the mass-weighted normal mode that needs to be characterized (dimension $3N$). After scaling, the square of each component forms a measure for the contribution of the respective translation or rotation to the normal mode.

We choose a logical scaling, so that the sum of the contributions of the translations and rotations of the building blocks and the contribution of the internal vibrations add up to 1. For that purpose, we have defined a collectivity factor. It is determined by the sum of the dot products of all mass-weighted reduced normal modes in the original basis with the original mass-weighted normal mode of interest. In this way, the collectivity factor determines the RUM character and quantifies the amount of translations and rotations of all the building blocks in the normal mode (1 means only translations and rotations, 0 means only internal vibrations). Subsequently, the contribution of the internal vibrations can thus be set to 1 - collectivity factor. Furthermore, the contributions of the translations and rotations of the building blocks are obtained by dividing the square of each component by the sum of all squares and multiply it with the collectivity factor.

It is clear that the above procedure is one of the many possible ways to quantify the mode character. Different variations exist, but the use of mass-weighted normal modes and mass-weighted translations and rotations vectors is natural, because the former are already orthonormal and the latter can be made orthonormal when the building blocks have no shared atoms in common and when the translation and rotation axes coincide with the inertia axes. In that case, the 'trick' with the collectivity factor is not necessary, because the sum of the squares of each component will already add up to 1 if the normal mode exist of only translations and rotations. In any case, each quantification procedure will lead to results that are qualitatively similar.

## S5.2 Mode character of low-frequency modes in MIL-53(Al)

We will illustrate the application of the above procedure on the low-frequency modes in the lp phase of MIL-53(Al). Figure S10 shows the resulting mode character of the 50 normal modes with the lowest vibrational frequencies, including the three pure translational modes with frequency 0 $\mathrm{cm}^{-1}$. The following 15 normal modes with the lowest frequencies all have a RUM character above 85% and are discussed in the main manuscript. It is clear that the other normal modes have a substantially lower RUM character, except for 4 normal modes inducing either shearing of the linkers in the direction of the 1D chain (at 131 and 133 $\mathrm{cm}^{-1}$) or in-plane rotation of the linker accompanied by rotation of the metal-oxide units (at 173 and 186 $\mathrm{cm}^{-1}$). The apparently high RUM character is partly artificial and originates from an annihilation of displacements of the hydroxyl group that serve as hinge atoms (see Figure S11 for a visualization).

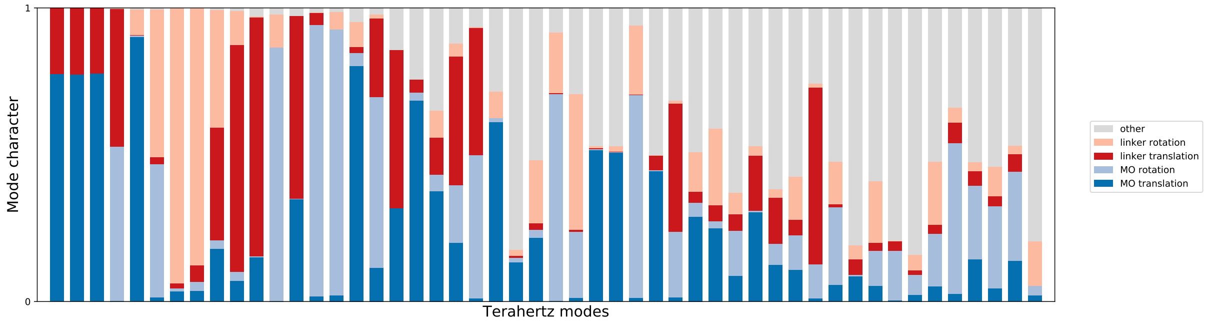

**Figure S10:** Mode character of the 50 eigenmodes with the lowest frequencies in the lp phase of MIL-53(Al)

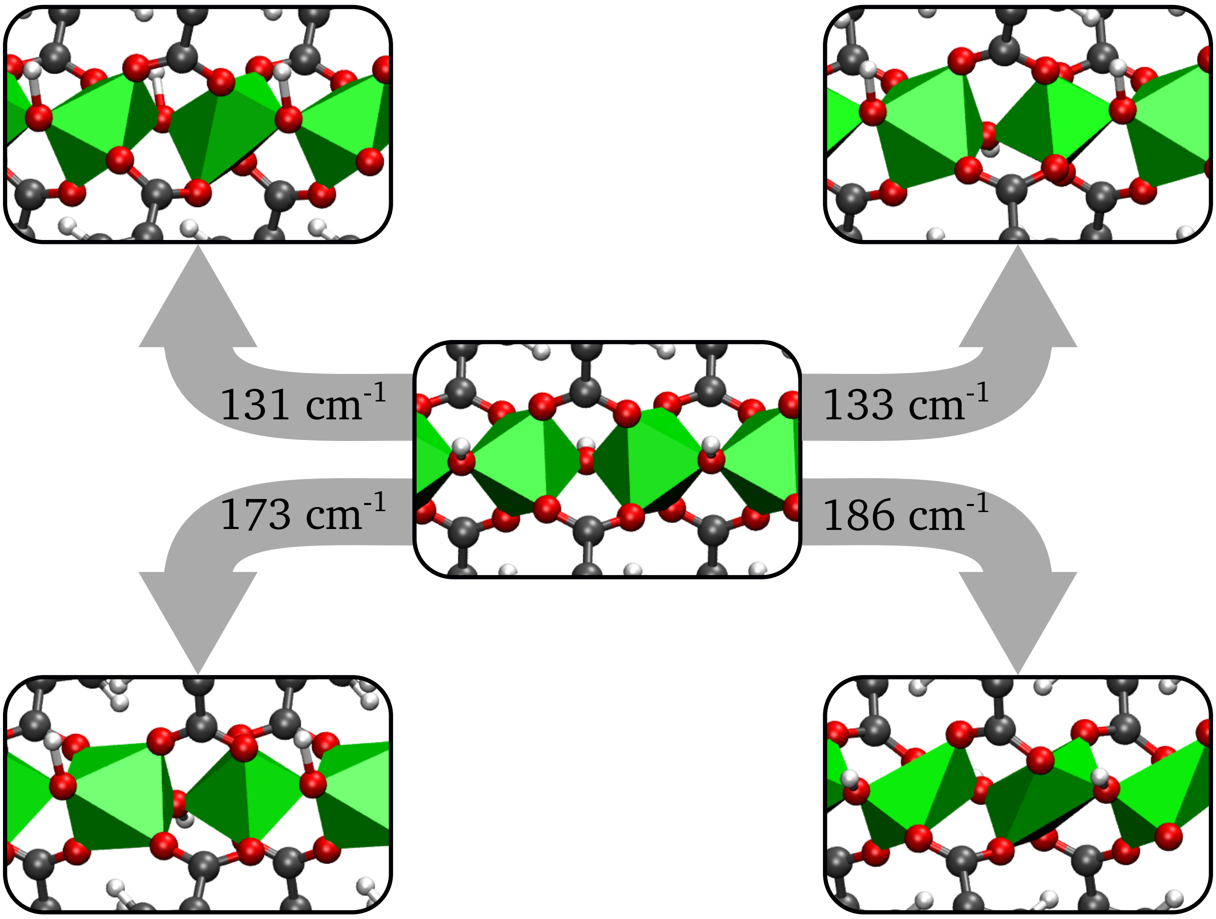

**Figure S11:** Visualization of low-frequency modes in MIL-53(Al) that have a high RUM character resulting from annihilation of displacements of the shared hydroxyl group.

## S5.3 Mode character in MIL-53-type materials

Following the above procedure, the mode character of the RUMs defined in the main manuscript can be determined in both the lp and cp phase. In the following, it is visualized for all studied MIL-53-type materials.

### Mode character in lp phase structures

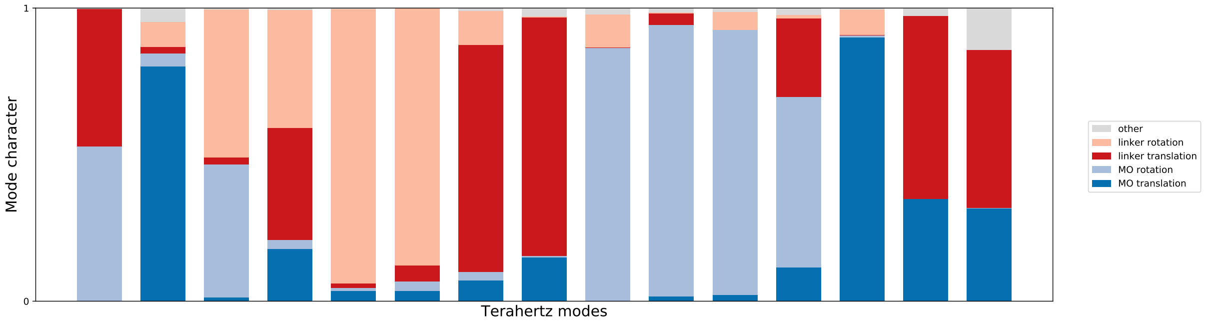

**Figure S12:** Mode character of the lp phase of MIL-53(Al)

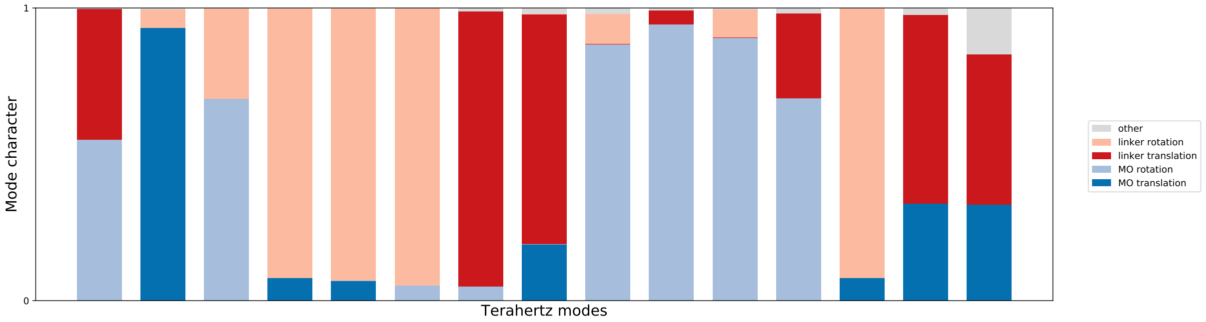

**Figure S13:** Mode character of the lp phase of MIL-53(Al)-F

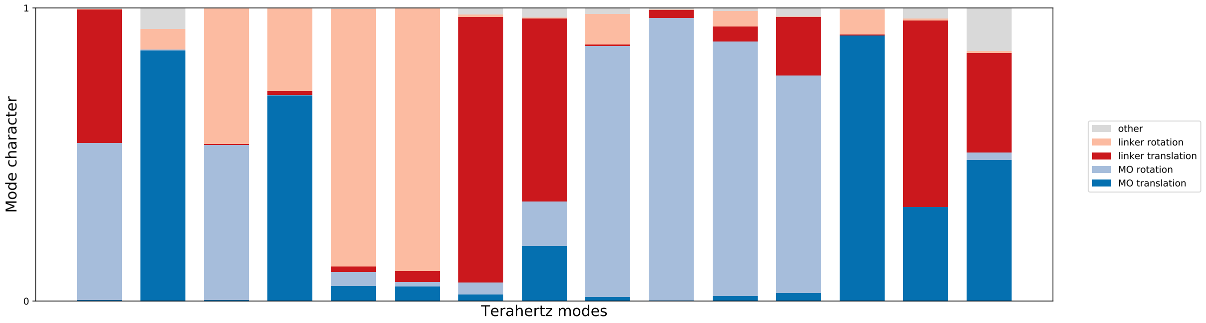

**Figure S14:** Mode character of the lp phase of MIL-47(V)

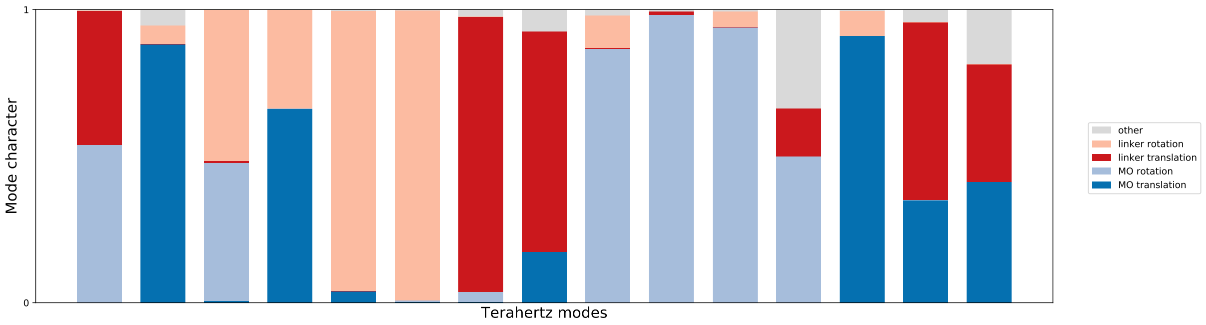

**Figure S15:** Mode character of the lp phase of MIL-53(V)

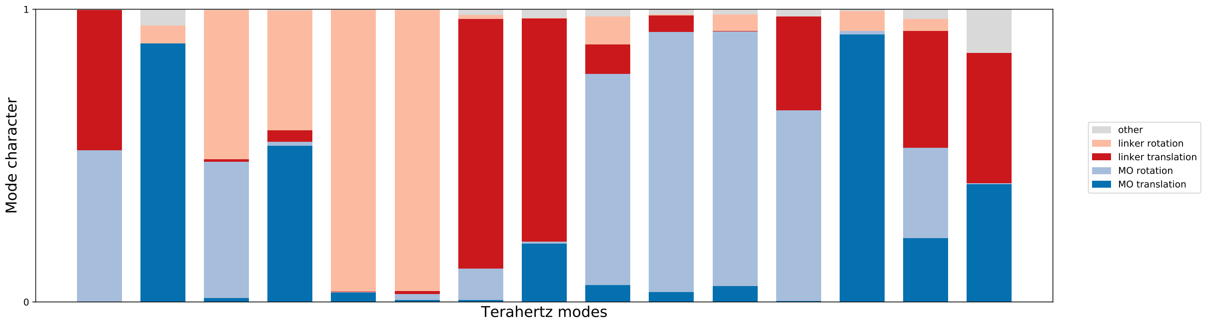

**Figure S16:** Mode character of the lp phase of MIL-53(Cr)

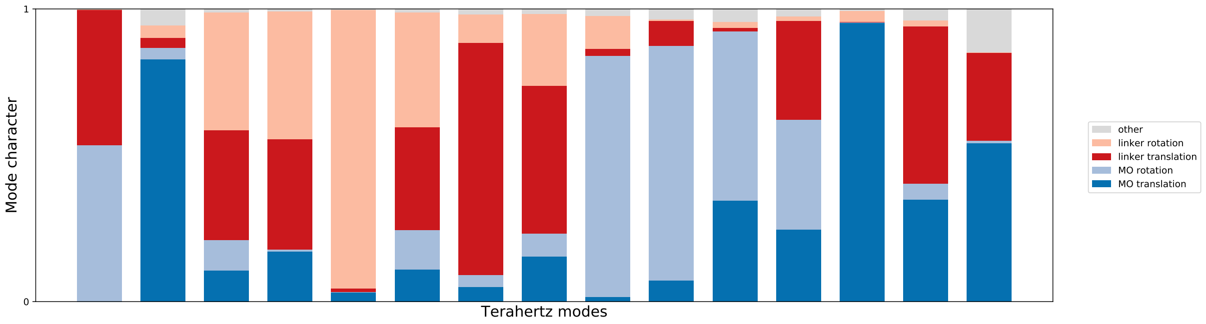

**Figure S17:** Mode character of the lp phase of MIL-53(Ga)

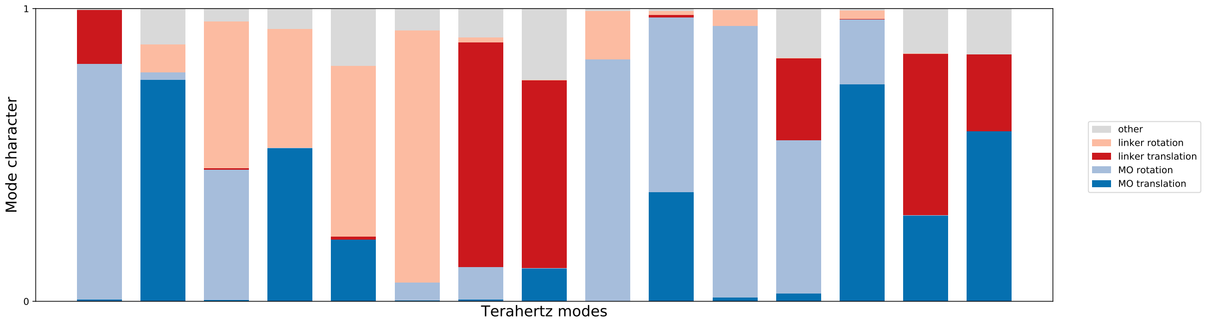

**Figure S18:** Mode character of the lp phase of A520(Al)

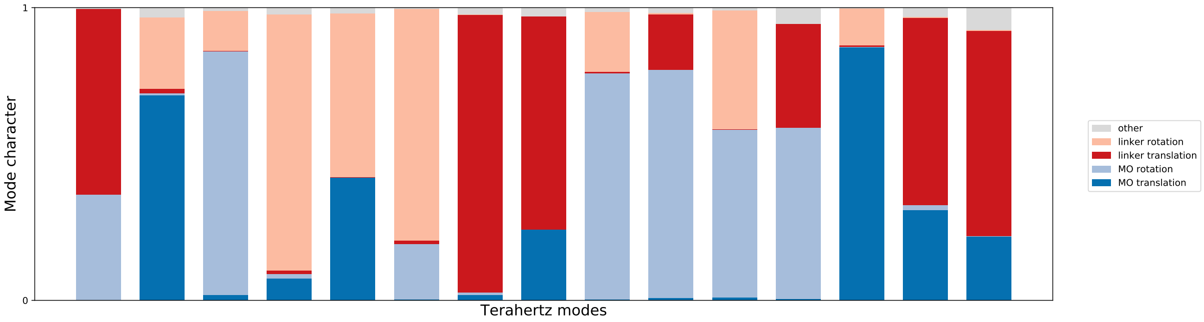

**Figure S19:** Mode character of the lp phase of DUT-4(Al)

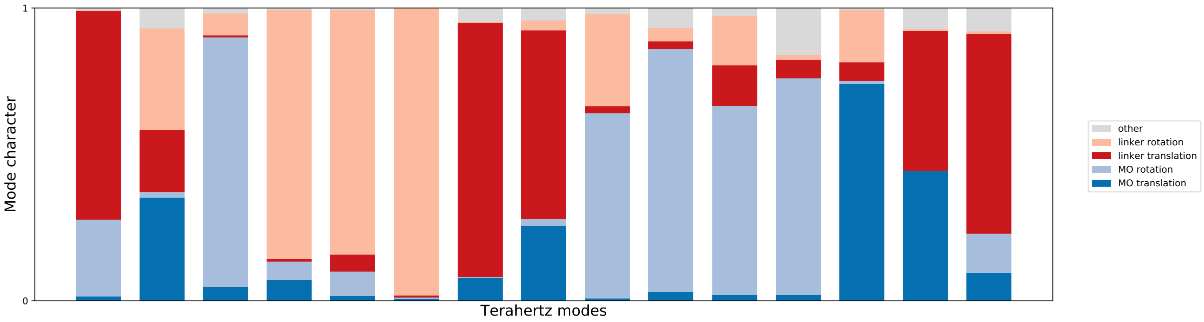

**Figure S20:** Mode character of the lp phase of DUT-5(Al)

## Mode character in cp phase structures

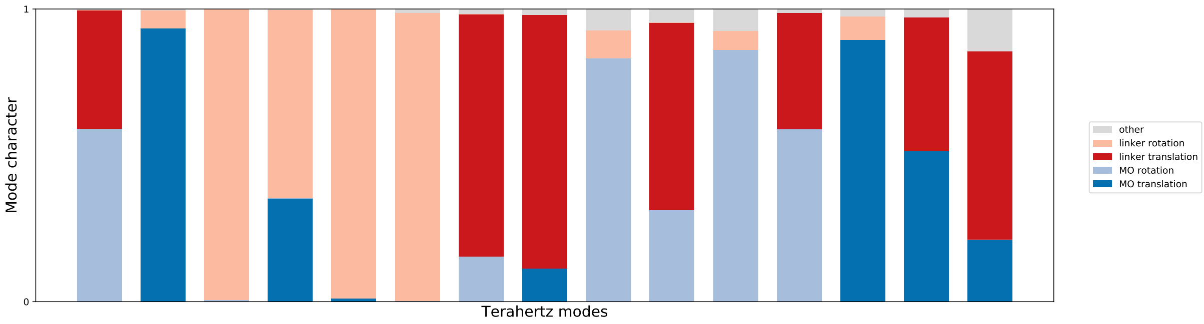

**Figure S21:** Mode character of the cp phase of MIL-53(Al)

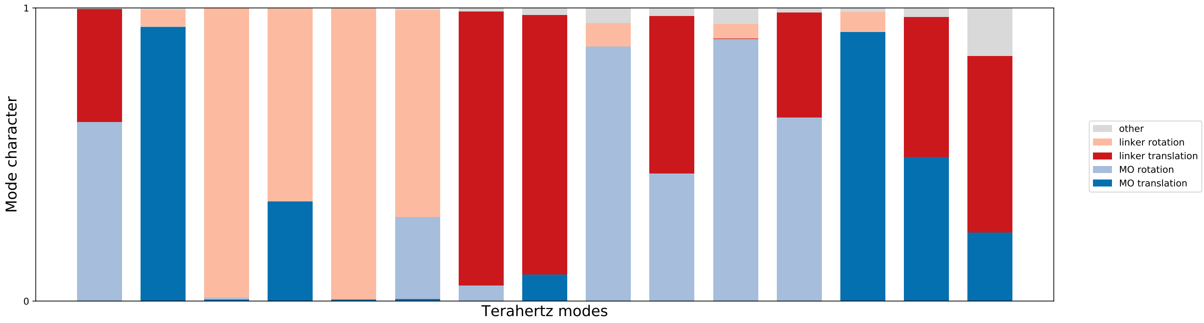

**Figure S22:** Mode character of the cp phase of MIL-53(Al)-F

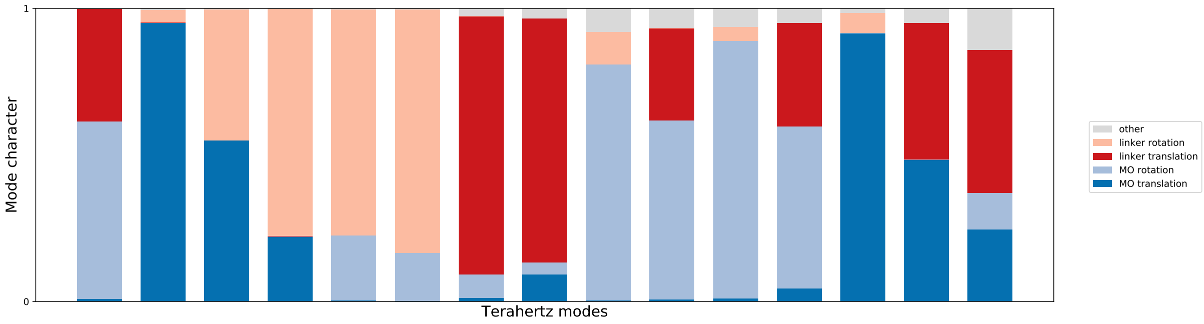

**Figure S23:** Mode character of the cp phase of MIL-47(V)

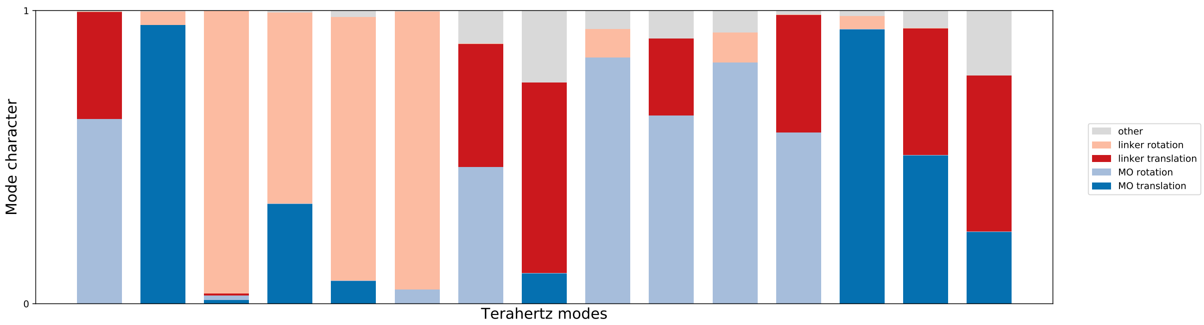

**Figure S24:** Mode character of the cp phase of MIL-53(V)

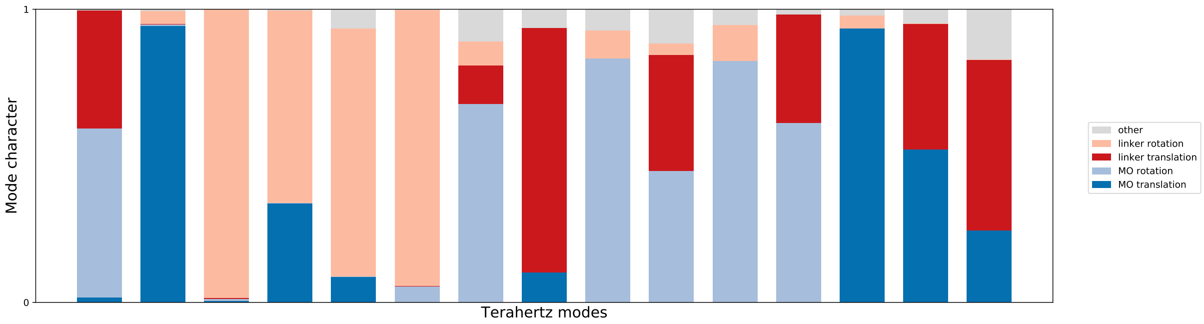

**Figure S25:** Mode character of the cp phase of MIL-53(Cr)

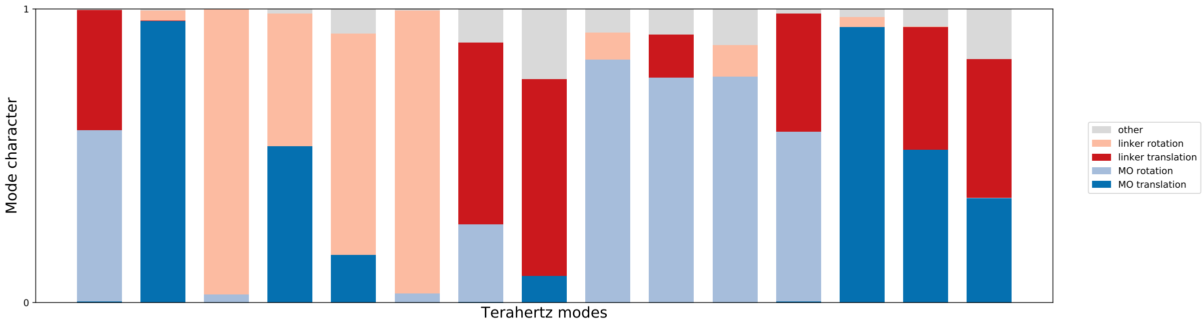

**Figure S26:** Mode character of the cp phase of MIL-53(Ga)

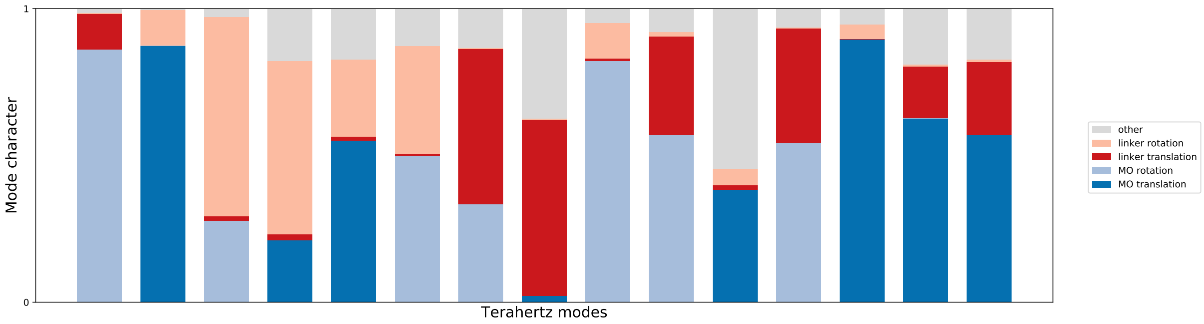

**Figure S27:** Mode character of the cp phase of A520(Al)

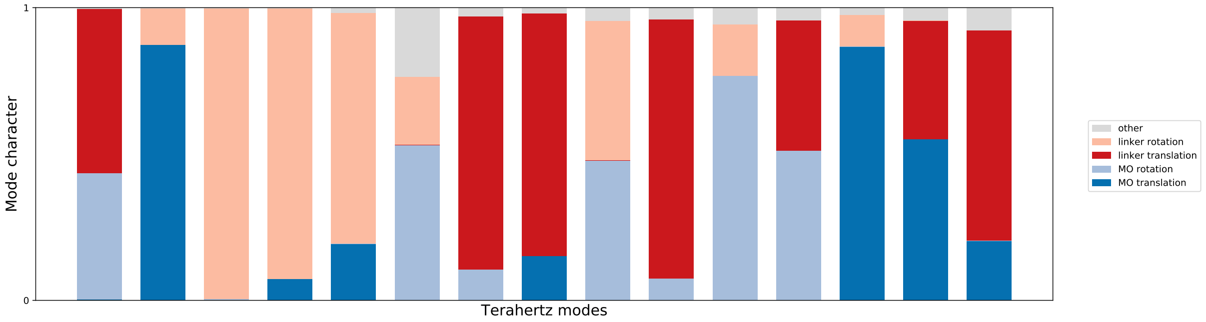

**Figure S28:** Mode character of the cp phase of DUT-4(Al)

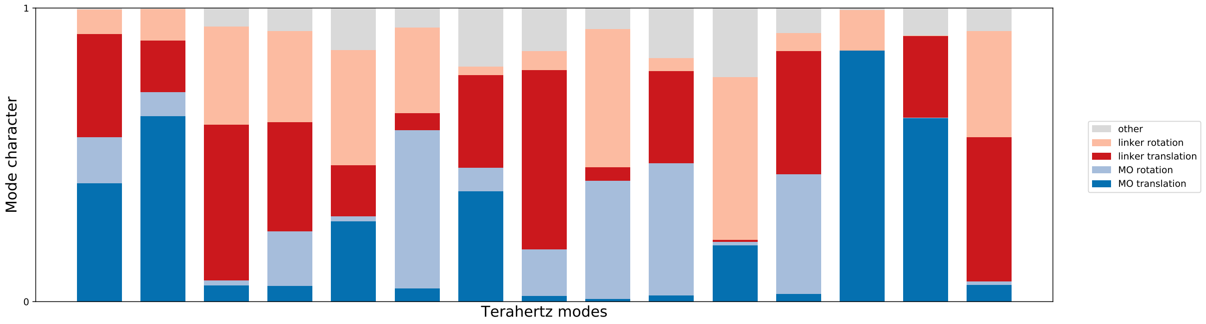

**Figure S29:** Mode character of the cp phase of DUT-5(Al)

## S6 Schematic visualization of RUMs

The nature of the RUMs identified in this paper only dependent on the topology and not on the specific building blocks. Therefore, these modes can be visualized schematically with general building blocks. In the main manuscript, a schematic representation was given for one mode of every specific group of vibrations. The visualization of the other RUMs will be presented here. The labeling of the different modes is defined in Figure S30.

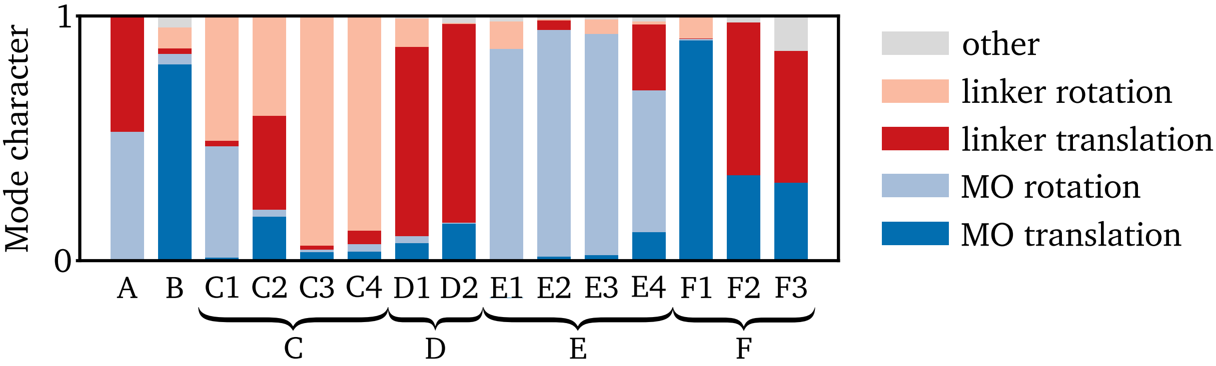

**Figure S30:** Mode character of the RUMs in the lp phase of MIL-53(Al) each with their own unique label

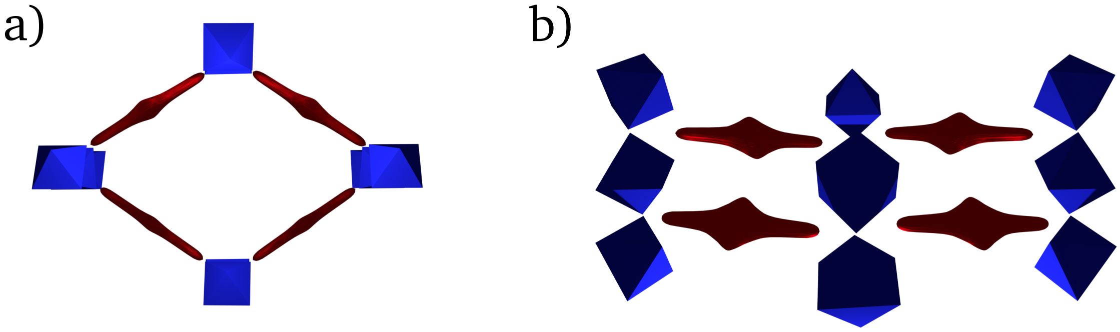

**Figure S31:** Schematic visualization of the MIL-53 topology in equilibrium. (a) View on the 1D channel. (b) View on the 1D chain.

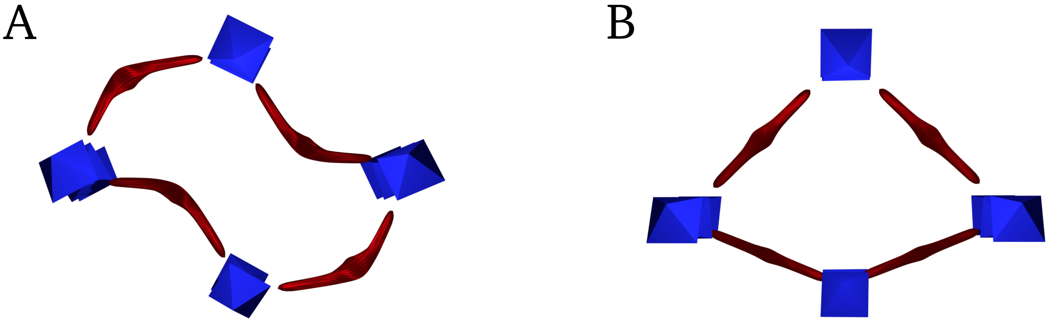

**Figure S32:** Schematic visualization of the soft modes in the MIL-53 topology

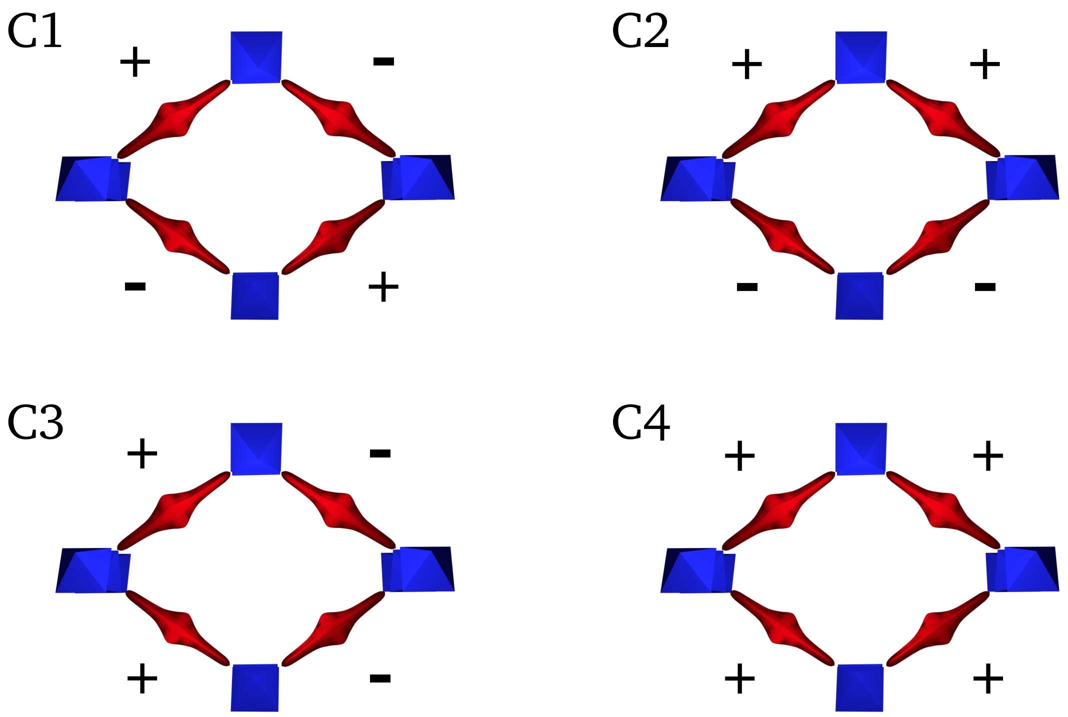

**Figure S33:** Schematic visualization of the modes inducing linker rotations in the MIL-53 topology. A + or - sign indicates whether the rotation around the axis occurs in the positive or negative sense, respectively.

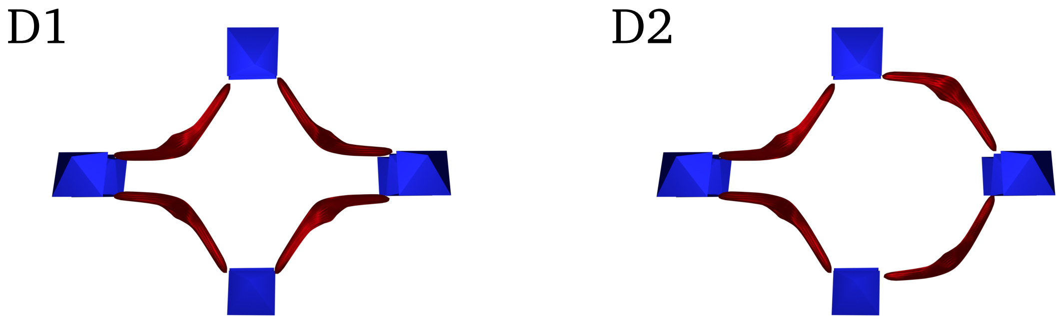

**Figure S34:** Schematic visualization of the modes inducing translations of the linkers in the MIL-53 topology

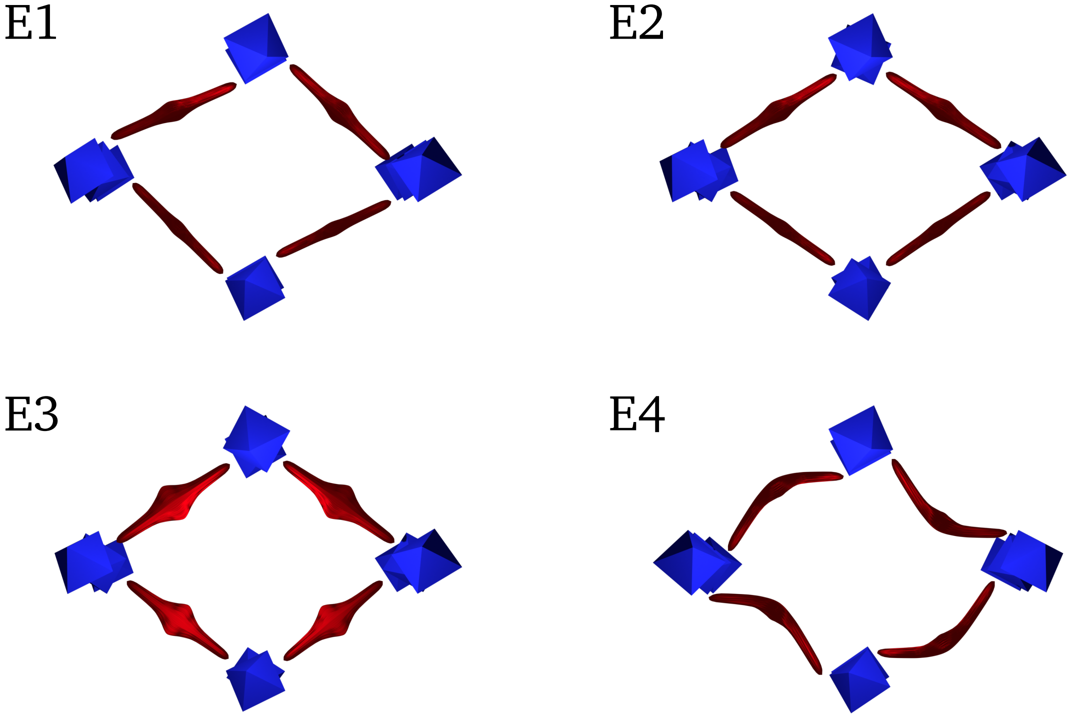

**Figure S35:** Schematic visualization of the modes inducing rotations of the metal-oxide units in the MIL-53 topology

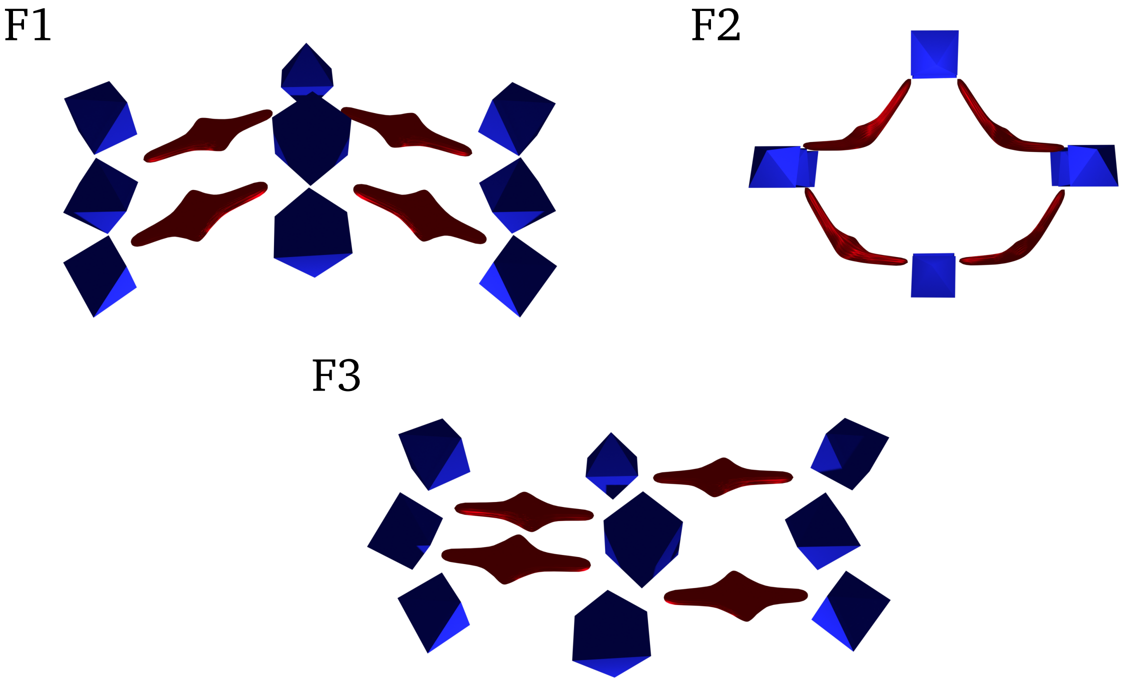

**Figure S36:** Schematic visualization of the shearing type modes in the MIL-53 topology

## S7 Detailed discussion of effect of linker substitution on RUMs

In the main manuscript, the general trends of linker substitution on the RUM frequencies were discussed. This section will be devoted to a more in-depth analysis of the RUM frequency differences. For the RUM inducing metal-oxide rotations and linker translations (mode A), the use of fumarate strongly increases the frequency difference, indicating that the mode becomes less soft in the cp phase. Other linkers leave this difference unaffected. The RUM characterized by metal-oxide translations and linker rotations (mode B) had a much lower vibrational frequency in the cp phase of MIL-53(Al) than in its lp phase. By substitution of BDC by fumarate or NDC, the frequency difference between both phases does even increase, although it has a distinct origin. In A520(Al), the increase is entirely the result of the higher vibrational frequency in the lp phase, whereas in DUT-4(Al) the increase is due to a lower frequency in the cp phase. The RUM in the cp phase of DUT-4(Al) becomes very soft (16 $\mathrm{cm}^{-1}$ compared to 30 $\mathrm{cm}^{-1}$ in MIL-53(Al)) and yields a major contribution to the vibrational entropy. The frequency difference of this RUM is substantially lower in DUT-5(Al). However, this is the result of a lower vibrational frequency in the lp phase, as the cp phase frequency is 14 $\mathrm{cm}^{-1}$, making it even softer than in DUT-4(Al). Therefore, the difference in frequency is still relatively high and will strongly influence the breathing behavior.

The terahertz vibrations exhibiting linker rotations (modes C) are split up in two groups. For the rotations of opposite linkers in the opposite sense, the modes in the cp phase are found at almost the same frequencies as in the lp phase, except for one mode in A520, where the cp phase frequency is much higher. However, as these type of vibrations have a relatively high frequency in both phases, their impact on a possible phase transition is limited. The second type of rotations, where the rotation takes place in the same sense, yield deviating frequency differences for DUT-4(Al) due to the disalignment of the carboxyl groups. For this structure, the modes in the cp and lp phase have comparable frequencies, reducing the entropic trigger to transition towards the lp phase, making it more rigid.

The disalignment of the NDC linker (see Section S3) does not affect the RUMs inducing translations of the linker in direction of the pore (modes D). Therefore, its frequency difference is comparable to MIL-53(Al), which is also the case for A520. Nevertheless, the absolute frequencies did change due to the different size of the linkers. In contrast, for DUT-5(Al) there is a large increase in the frequency difference compared to the other structures. The frequency in its cp phase did not decrease because the effect of the bigger linker was compensated by repulsive interactions upon linker translation. Hence, this RUM forms a strong entropic trigger to transition to the lp phase in DUT-5(Al).

The last RUMs leading to substantial frequency differences between the cp and lp phase show rotations of the metal-oxide units (modes E). When all the metal-oxide units rotate in the same sense, linker substitution has no profound influence. However, when neighboring metal-oxide units rotate in the opposite sense the fumarate linker strongly increases the frequency difference, because these RUMs have a higher vibrational frequency in the cp phase and a lower one in the lp phase. One of the two RUMs even has a frequency of 27 $\mathrm{cm}^{-1}$ in the latter phase, making it very soft. Consequently, these modes entropically favor the lp phase in A520(Al) to a great extent. The same holds for DUT-5(Al) with the BPDC linker, although the frequency difference is lower. Unlike fumarate and BPDC, substitution with the NDC linker decreases the frequency difference due to a lower vibrational frequency of these RUMs in the cp phase. Apparently, the disalignement of the linkers facilitates these type of modes in the dense structure.

As a final note, it can be observed that also linker substitution will not affect the frequency difference between the two phases for the shearing type vibrations (modes F), although it did change their frequencies in the separate phases. As a result, these RUMs play no role in the breathing mechanism.

## S8 Visualization of linker orientation in lp phase of MIL-53(V)

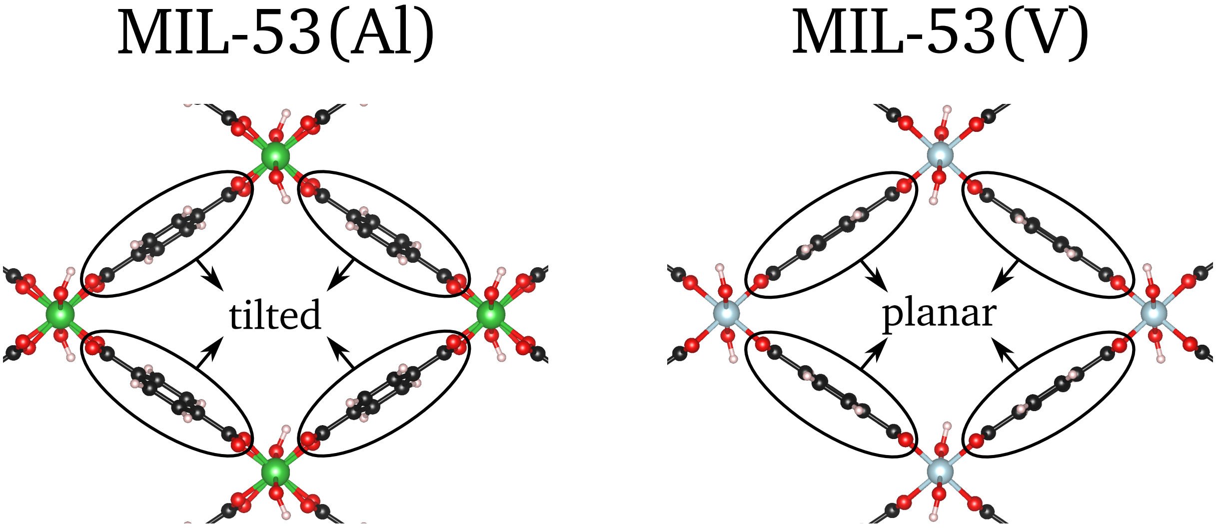

**Figure S37:** visualization of the lp phase of MIL-53(Al) with tilted linkers and MIL-53(V) with planar linkers

## S9 Volume-frequency relations of MIL-53(Al), MIL-53(Ga), and MIL-47(V)

In the main manuscript, it is stated that the difference in vibrational frequency of the vibrations inducing linker rotations (type C) and those inducing linker translations (type D) between MIL-53(Al) and MIL-47(V) in their cp phases is almost entirely the result of the increased equilibrium volume in the latter material. This becomes clear when analyzing the frequency as a function of the unit cell volume of these modes (see Figure S38). It is indeed true that the volume-frequency relations of modes C1, C3, and D2 almost completely coincide, except at very large volumes. In contrast, the volume frequency relations of the soft modes (A and B) and the vibrations inducing rotations of the metal-oxide unit (E1) depend on the choice of the metal-oxide unit. In Figure S38 also the volume-frequency relations of MIL-53(Ga) are included to show that this observation is not restricted to MIL-53(Al) and MIL-47(V).

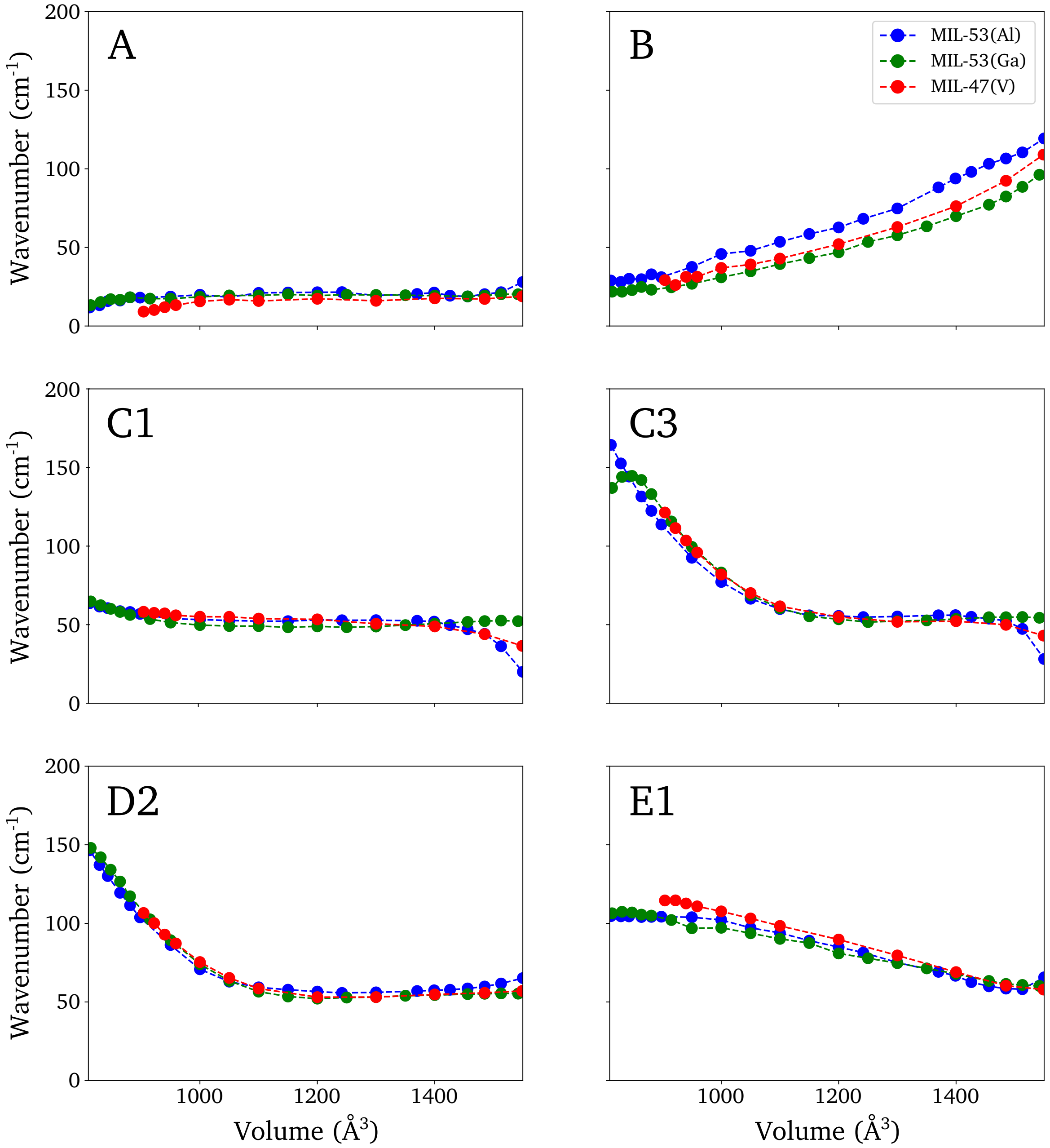

**Figure S38:** Volume-frequency relation of six RUMs for MIL-53(Al), MIL-53(Ga), and MIL-47(V). The mode labels are the ones defined in Figure S30.

## S10 Free energy and entropy

The free energy determines the stability of the structure and can be defined via the internal energy, $E$, and the entropy, $S$:

$$F(T) = E(T) - TS(T) \tag{4}$$

In the quantum-harmonic approximation $E$ and $S$ follow from the normal mode frequencies:

$$E(T) = E_{el} + \sum_{i=1}^{3N} \left( \frac{\hbar\omega_i}{2} + \frac{\hbar\omega_i}{\exp\left(\frac{\hbar\omega_i}{k_B T}\right) - 1} \right) \tag{5}$$

$$S(T) = k_B \sum_{i=1}^{3N} \left( \frac{\frac{\hbar\omega_i}{k_B T}}{\exp\left(\frac{\hbar\omega_i}{k_B T}\right) - 1} - \ln\left[1 - \exp\left(-\frac{\hbar\omega_i}{k_B T}\right)\right] \right) \tag{6}$$

with $E_{el}$ the electronic energy, $\hbar$ planck's constant, $k_B$ boltzmann's constant, and $\omega_i$ the angular frequency of normal mode $i$. Consequently, $F$ can be written as:

$$F(T) = E_{el} + \sum_{i=1}^{3N} \left( \frac{\hbar\omega_i}{2} + k_B T \ln\left[1 - \exp\left(-\frac{\hbar\omega_i}{k_B T}\right)\right] \right) \tag{7}$$

The latter term in the expression for the free energy is an entropy term and is largest for normal modes with the lowest frequencies. Therefore, the RUMs largely determine the entropic contribution to the free energy. In Table S3, the free energy difference and the entropy difference between the lp and the cp phase at 100 K, 300 K, and 500 K are presented for the different MIL-53 analogs together with the electronic energy difference. In Figures S39 and S40, the free energy difference and the entropy difference between the lp and the cp phase for the different MIL-53 analogs are plotted as a function of temperature.

**Table S3:** Free energy difference and entropy difference ($T\Delta S$ term) (in kJ/mol) between the lp and cp phase at 100 K, 300 K, and 500 K for the different MIL-53 structures. All vibrational frequencies were taken into account. Also the electronic energy difference (in kJ/mol) is presented.

| | $\Delta E_{el}$ | $\Delta F_{100}$ | $T\Delta S_{100}$ | $\Delta F_{300}$ | $T\Delta S_{300}$ | $\Delta F_{500}$ | $T\Delta S_{500}$ |
|---|---|---|---|---|---|---|---|
| MIL-53(Al) | 26.7 | 23.7 | 2.7 | 17.6 | 9.5 | 11.3 | 15.7 |
| MIL-53(Ga) | 34.1 | 30.7 | 3.4 | 22.7 | 12.1 | 14.7 | 19.9 |
| MIL-53(Cr) | 27.5 | 21.9 | 3.7 | 13.5 | 13.1 | 4.7 | 22.1 |
| MIL-53(V) | 39.0 | 28.6 | 7.1 | 12.2 | 25.7 | -5.0 | 43.4 |
| MIL-53(Al)-F | 0.6 | -2.6 | 2.4 | -8.5 | 9.4 | -14.8 | 15.7 |
| MIL-47(V) | -3.0 | -7.6 | 3.9 | -16.5 | 14.0 | -25.9 | 23.5 |
| A520(Al) | -15.2 | -18.1 | 2.9 | -24.8 | 10.3 | -31.6 | 17.1 |
| DUT-4(Al) | 113.1 | 108.9 | 0.6 | 107.1 | 2.9 | 105.1 | 5.1 |
| DUT-5(Al) | 138.1 | 127.4 | 6.9 | 111.9 | 24.2 | 95.7 | 40.6 |

**Table S4:** Free energy difference and entropy difference ($T\Delta S$ term) (in kJ/mol) between the lp and cp phase at 100 K, 300 K, and 500 K for the different MIL-53 structures. Only RUM frequencies were taken into account. Also the electronic energy difference (in kJ/mol) is presented.

| | $\Delta E_{el}$ | $\Delta F_{100}$ | $T\Delta S_{100}$ | $\Delta F_{300}$ | $T\Delta S_{300}$ | $\Delta F_{500}$ | $T\Delta S_{500}$ |
|---|---|---|---|---|---|---|---|
| MIL-53(Al) | 26.7 | 22.8 | 2.8 | 16.5 | 9.8 | 10.0 | 16.5 |
| MIL-53(Ga) | 34.1 | 29.8 | 2.9 | 23.1 | 10.5 | 16.0 | 17.8 |
| MIL-53(Cr) | 27.5 | 22.4 | 3.5 | 14.4 | 12.5 | 6.0 | 21.2 |
| MIL-53(V) | 39.0 | 31.2 | 6.0 | 18.1 | 20.3 | 4.5 | 34.1 |
| MIL-53(Al)-F | 0.6 | -2.7 | 2.5 | -8.2 | 8.5 | -13.9 | 14.3 |
| MIL-47(V) | -3.0 | -7.2 | 3.3 | -14.5 | 11.2 | -21.9 | 18.7 |
| A520(Al) | -15.2 | -21.0 | 3.7 | -29.6 | 13.6 | -38.8 | 23.2 |
| DUT-4(Al) | 113.1 | 111.1 | 1.3 | 108.1 | 4.8 | 105.0 | 8.0 |
| DUT-5(Al) | 138.1 | 132.0 | 4.9 | 121.6 | 16.1 | 110.8 | 27.1 |

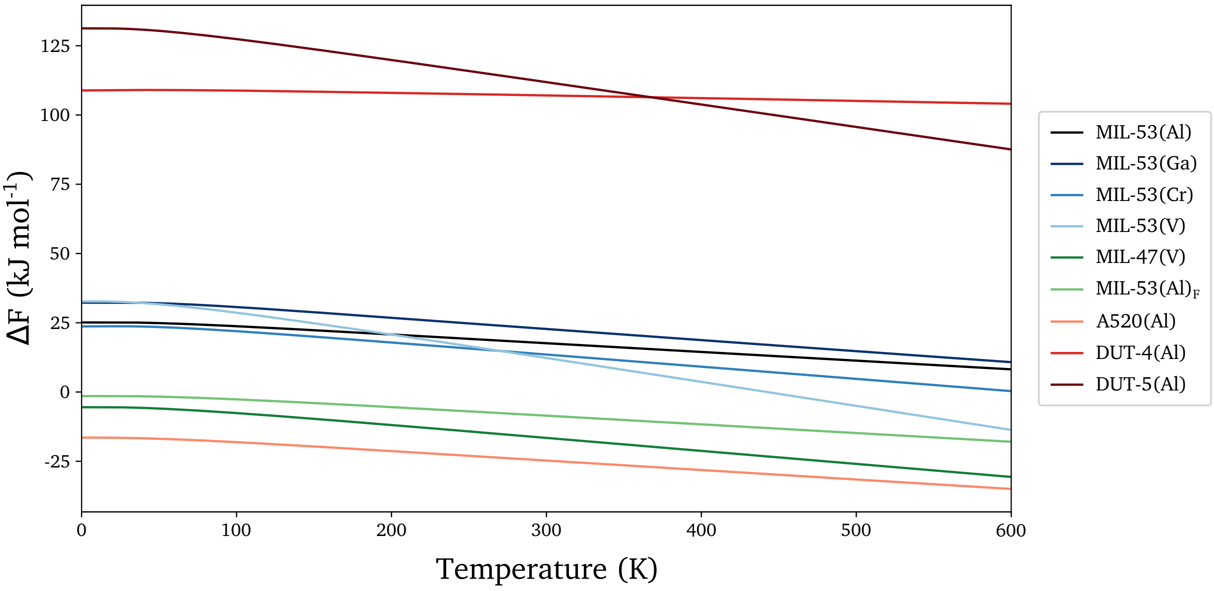

**Figure S39:** Free energy difference as a function of temperature for the different MIL-53 analogs

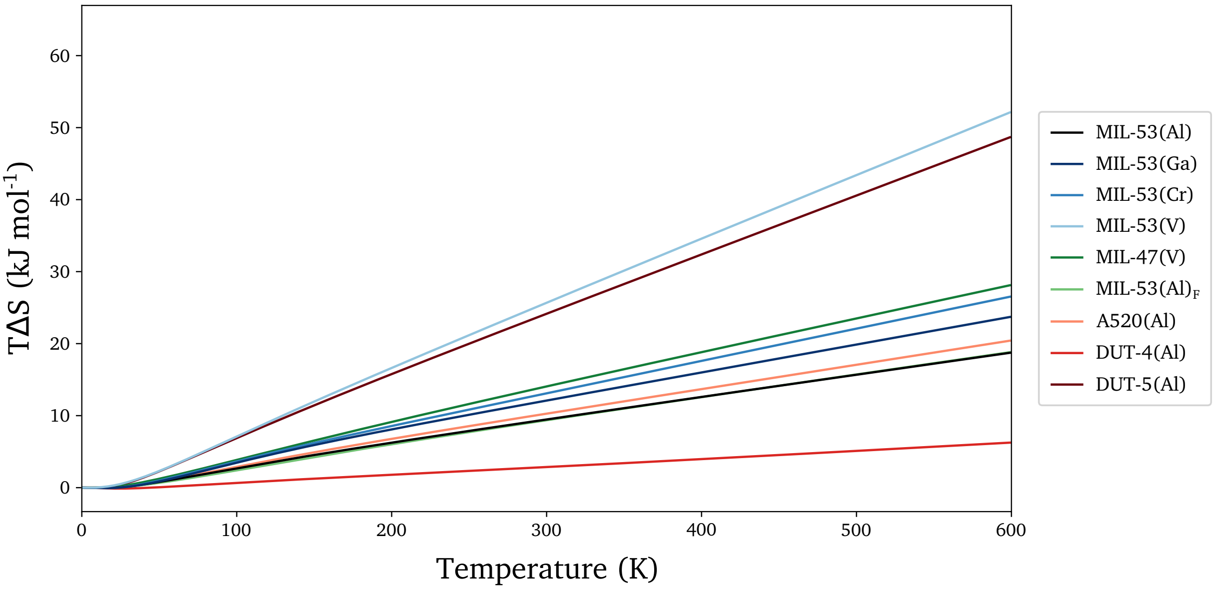

**Figure S40:** Entropy difference in terms of TΔS as a function of temperature for the different MIL-53 analogs

# S11 Impact of defects on phonon modes

The investigated winerack frameworks in this study were pristine structures without defects. However, experimental structures often contain defects to a certain degree. To estimate the effect of the presence of defects on the rigid unit modes, the vibrational spectrum of several defective structures will be studied in this section. Two types of defects will be highlighted: missing linker defects and a change in oxidation state. These two theoretical defects can be straightforwardly modeled and, in this way, the impact of alteration in, respectively, the organic linker and inorganic chain, will be determined.

## S11.1 Missing linker defect

A missing linker defect has been investigated for the structures MIL-53(Al), DUT-4(Al), and DUT-5(Al), consisting of, respectively, BDC, NDC, and BPDC linkers. To isolate the missing linker defect, a 2 × 1 × 1 supercell structure is considered extending the unit cell over the 1D inorganic chain. Moreover, the defect is introduced by removing the linker and terminating the carboxylic group with a hydrogen atom (formic acid) (see Figure S41 for a visualization). The geometry of the defective structure is optimized and the corresponding Hessian is calculated according to the procedure described in the manuscript. To facilitate a direct comparison of the phonon modes of the defective supercell structure with those of the pristine structure, the Hessian of the supercell structure of the latter has also been calculated. In the following the results for the lp (Figures S42, S43, S44, and S45) and cp (Figures S46 and S47) phase of MIL-53(Al), the lp phase of DUT-4(Al) (Figures S48 and S49), and the lp phase of DUT-5(Al) (Figures S50 and S51) are presented:

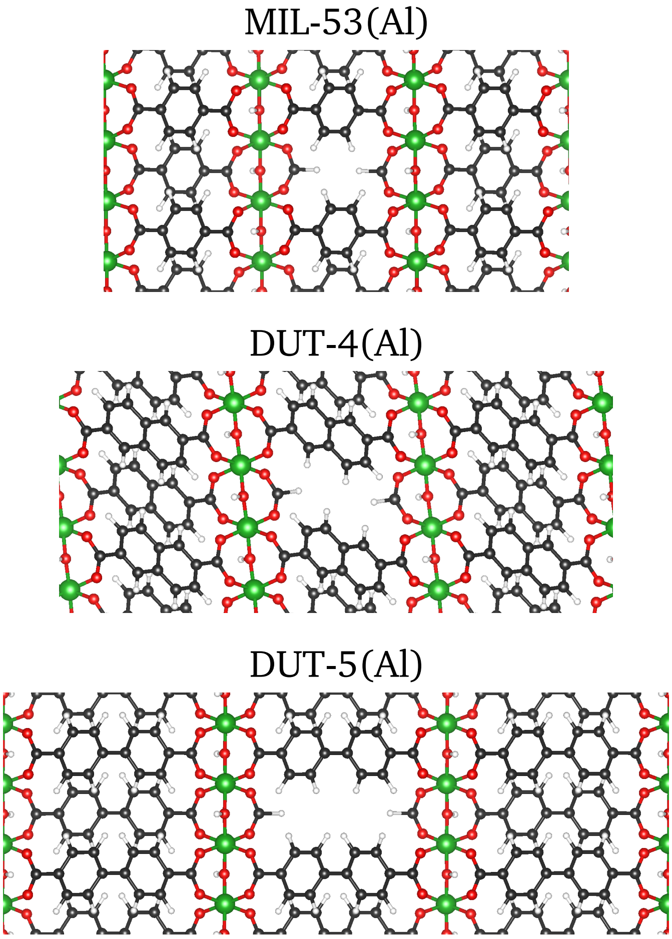

**Figure S41:** Visualization of the missing linker defect in MIL-53(Al), DUT-4(Al), and DUT-5(Al).

## MIL-53(Al)

### lp phase ($2 \times 1 \times 1$ supercell)

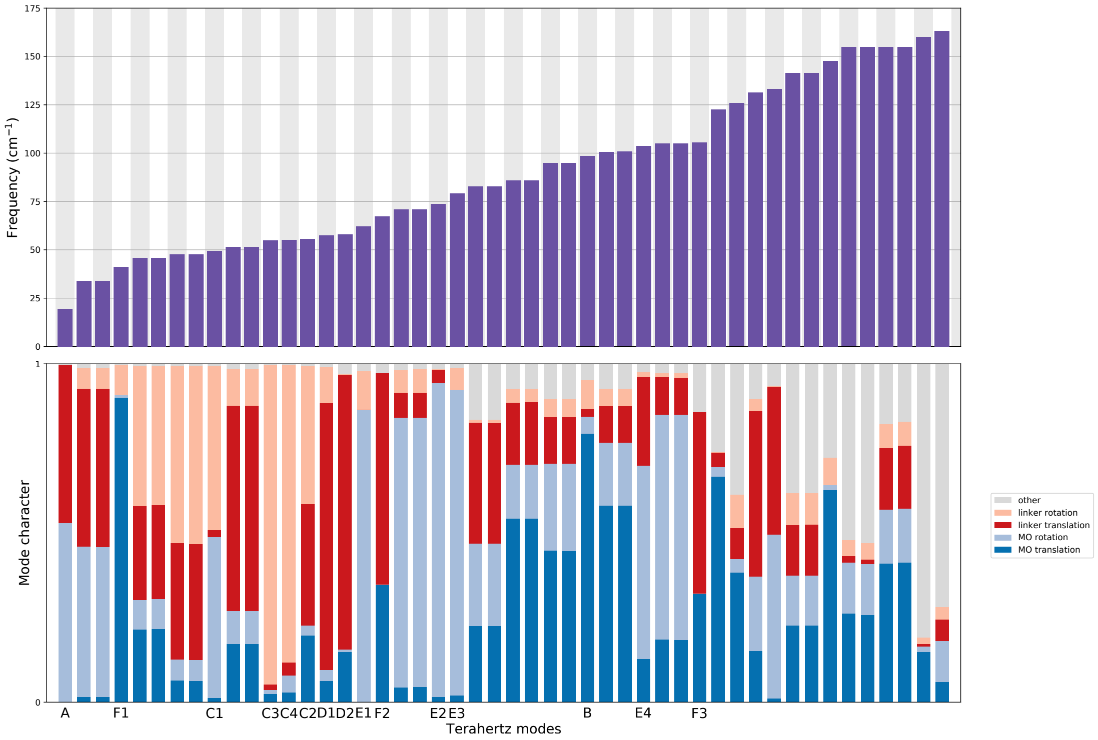

**Figure S42:** Mode frequency and character of the 48 phonon modes with the lowest frequency in the $2 \times 1 \times 1$ supercell of the lp phase of MIL-53(Al). The RUMs identified in the unit cell are indicated.

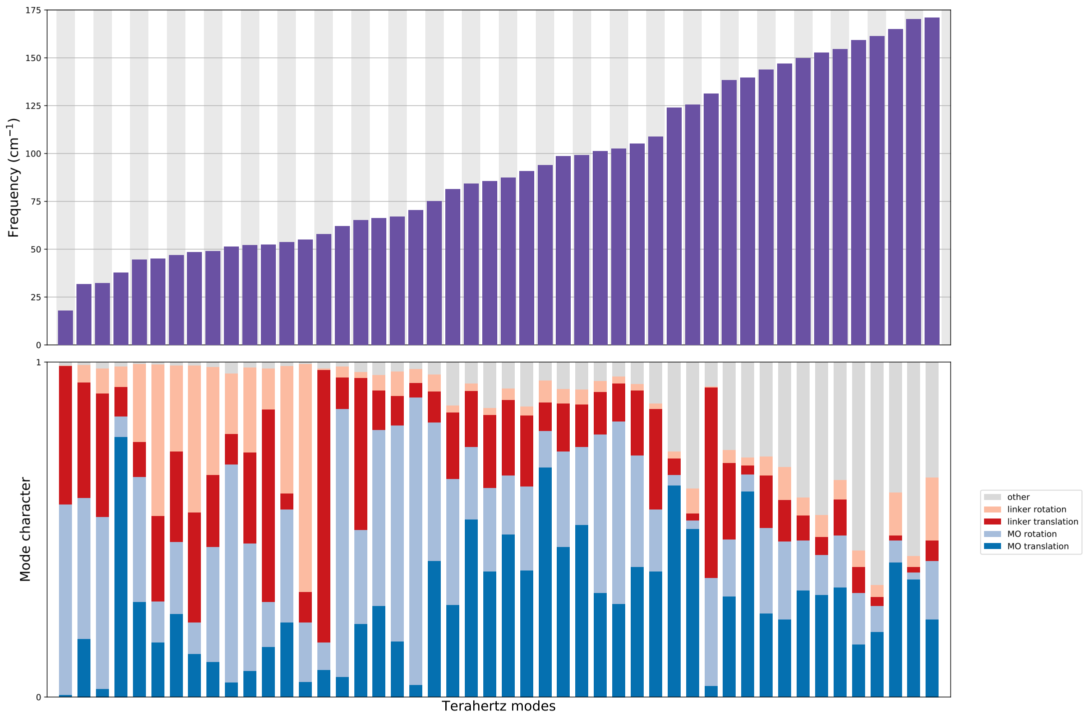

**Figure S43:** Mode frequency and character of the 48 phonon modes with the lowest frequency in the $2 \times 1 \times 1$ supercell of the lp phase of MIL-53(Al) containing a missing linker defect.

## lp phase ($3 \times 1 \times 1$ supercell)

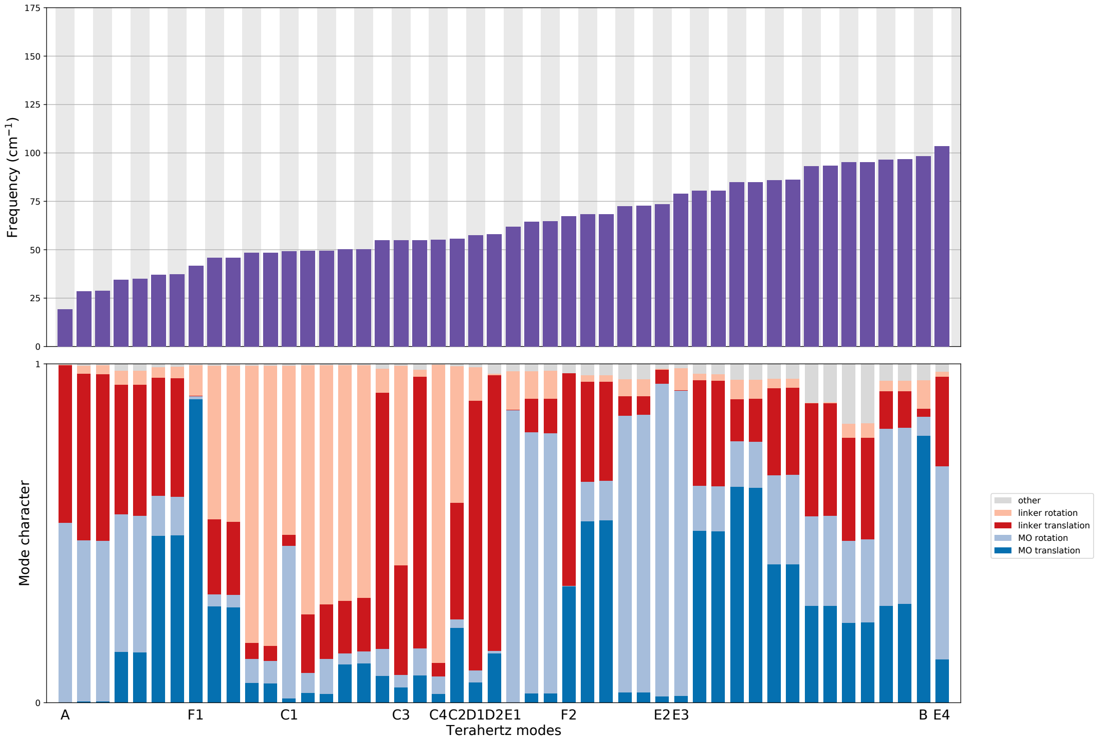

**Figure S44:** Mode frequency and character of the 48 phonon modes with the lowest frequency in the $3 \times 1 \times 1$ supercell of the lp phase of MIL-53(Al). The RUMs identified in the unit cell are indicated.

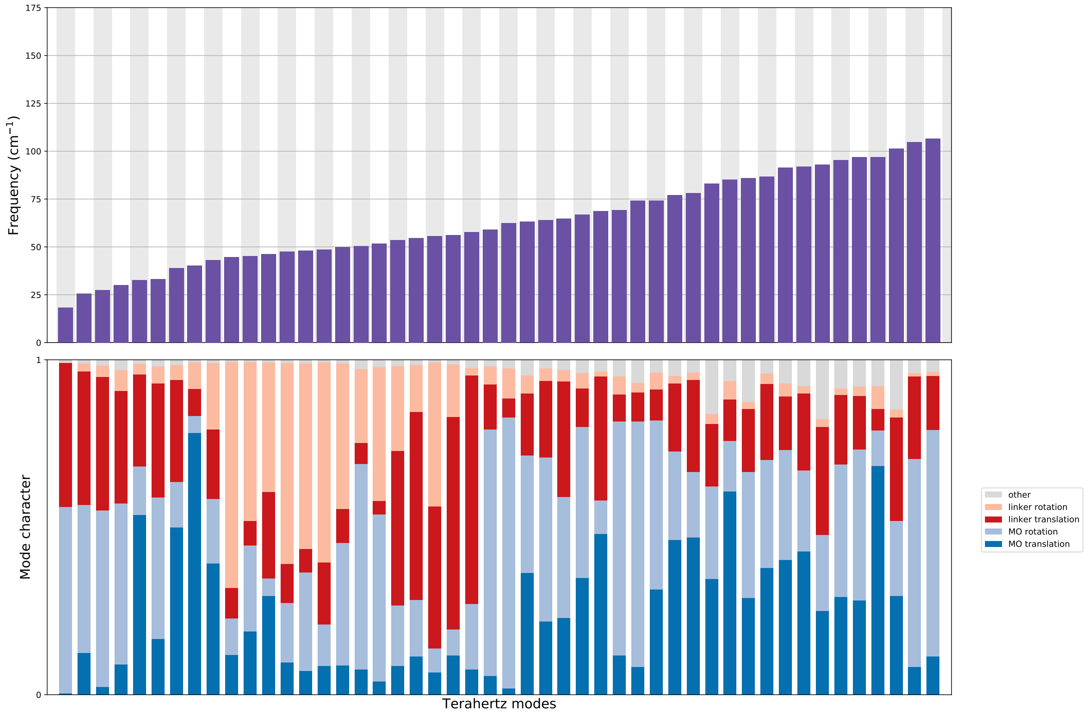

**Figure S45:** Mode frequency and character of the 48 phonon modes with the lowest frequency in the $3 \times 1 \times 1$ supercell of the lp phase of MIL-53(Al) containing a missing linker defect.

## cp phase

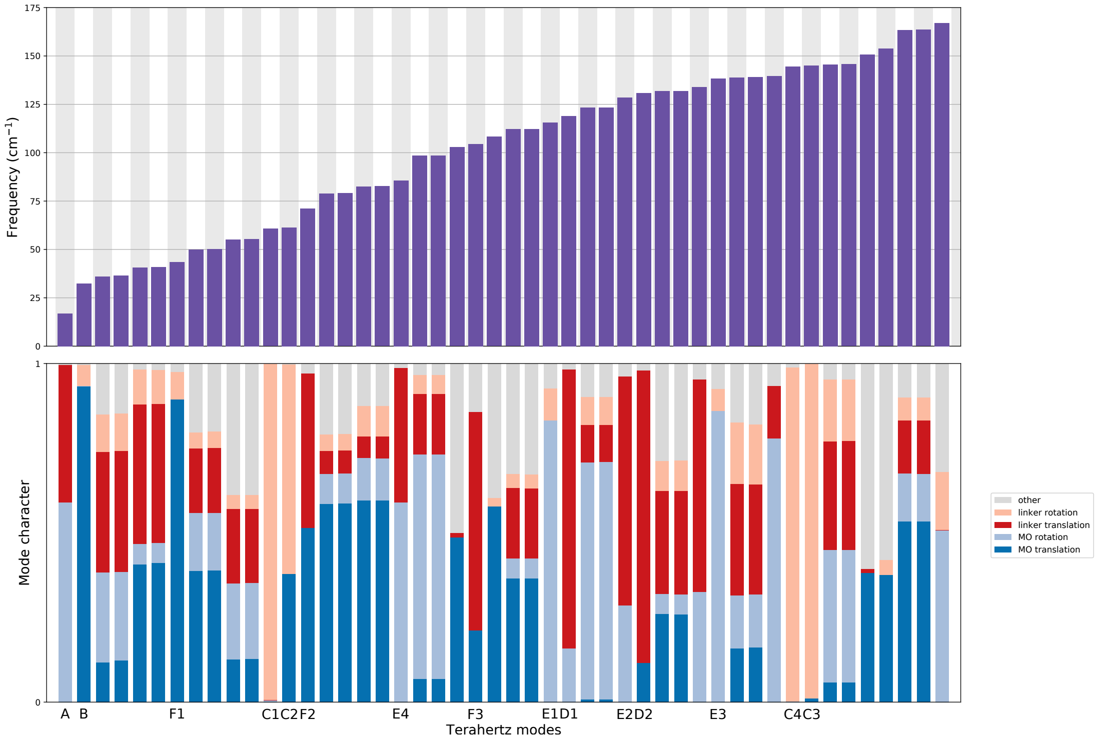

**Figure S46:** Mode frequency and character of the 48 phonon modes with the lowest frequency in the $2 \times 1 \times 1$ supercell of the cp phase of MIL-53(Al). The RUMs identified in the unit cell are indicated.

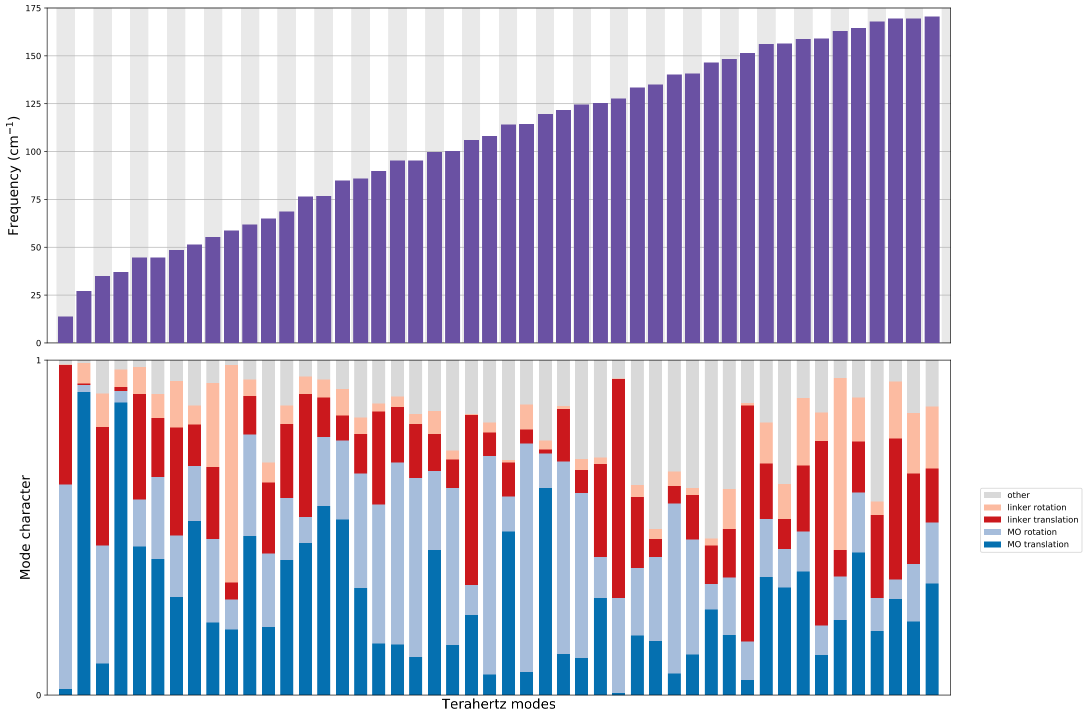

**Figure S47:** Mode frequency and character of the 48 phonon modes with the lowest frequency in the $2 \times 1 \times 1$ supercell of the cp phase of MIL-53(Al) containing a missing linker defect.

## DUT-4(Al)

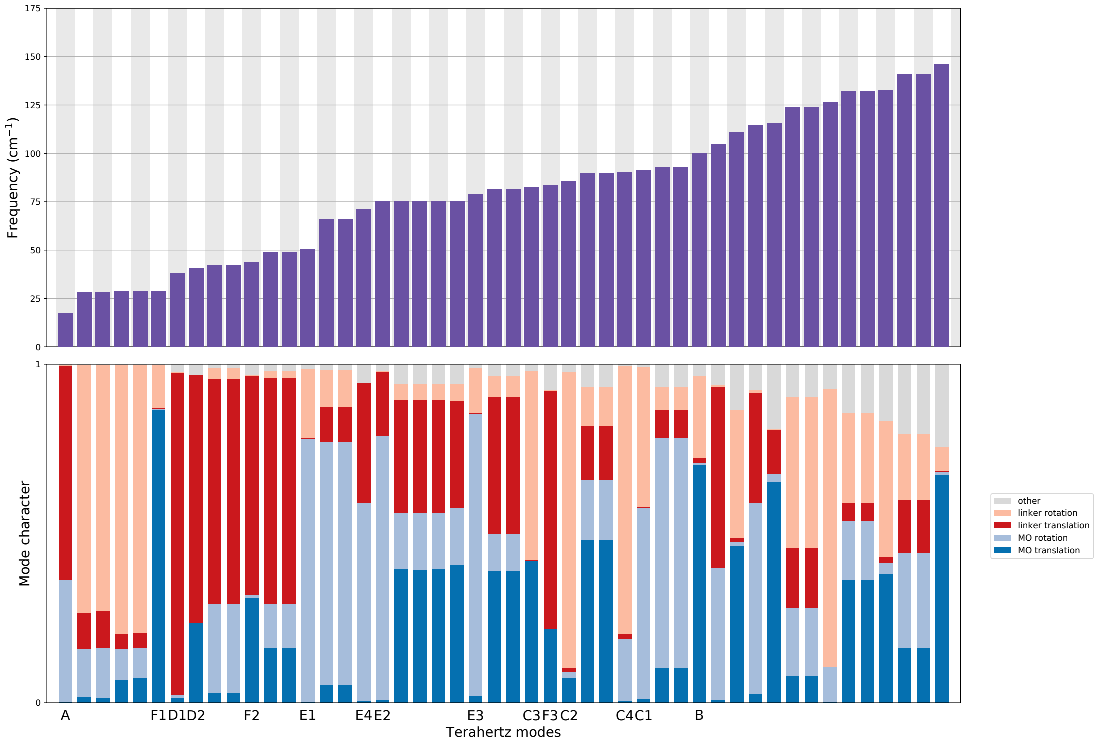

**Figure S48:** Mode frequency and character of the 48 phonon modes with the lowest frequency in the $2 \times 1 \times 1$ supercell of the lp phase of DUT-4(Al). The RUMs identified in the unit cell are indicated.

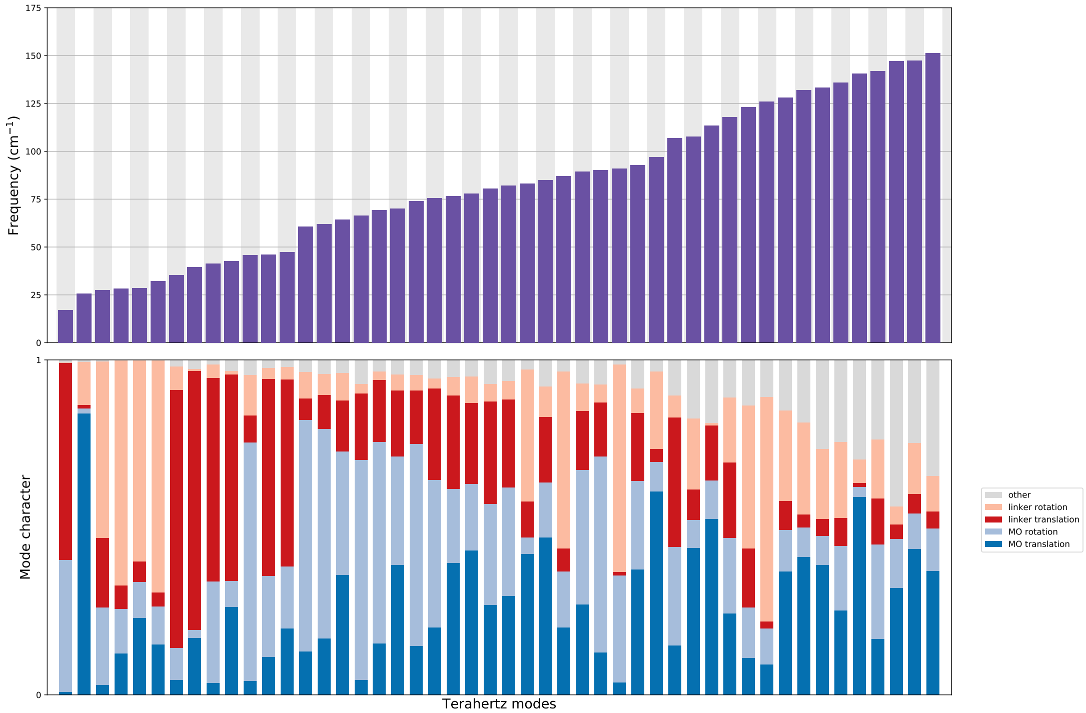

**Figure S49:** Mode frequency and character of the 48 phonon modes with the lowest frequency in the $2 \times 1 \times 1$ supercell of the lp phase of DUT-4(Al) containing a missing linker defect.

## DUT-5(Al)

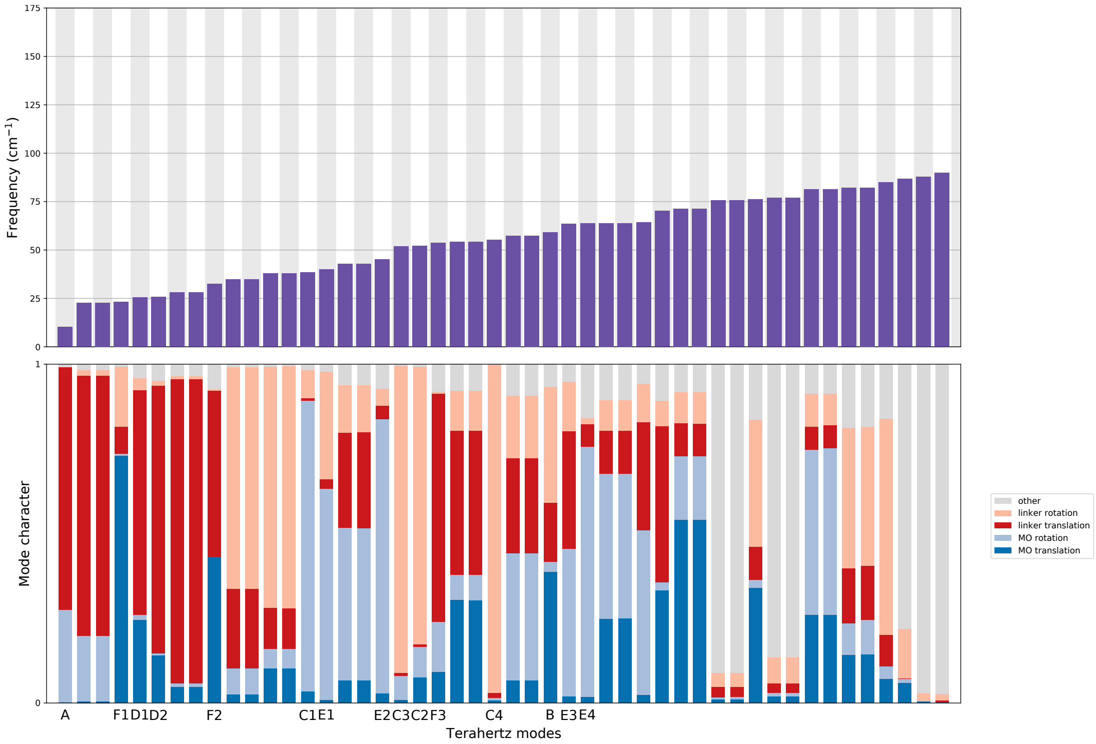

**Figure S50:** Mode frequency and character of the 48 phonon modes with the lowest frequency in the $2 \times 1 \times 1$ supercell of the lp phase of DUT-5(Al). The RUMs identified in the unit cell are indicated.

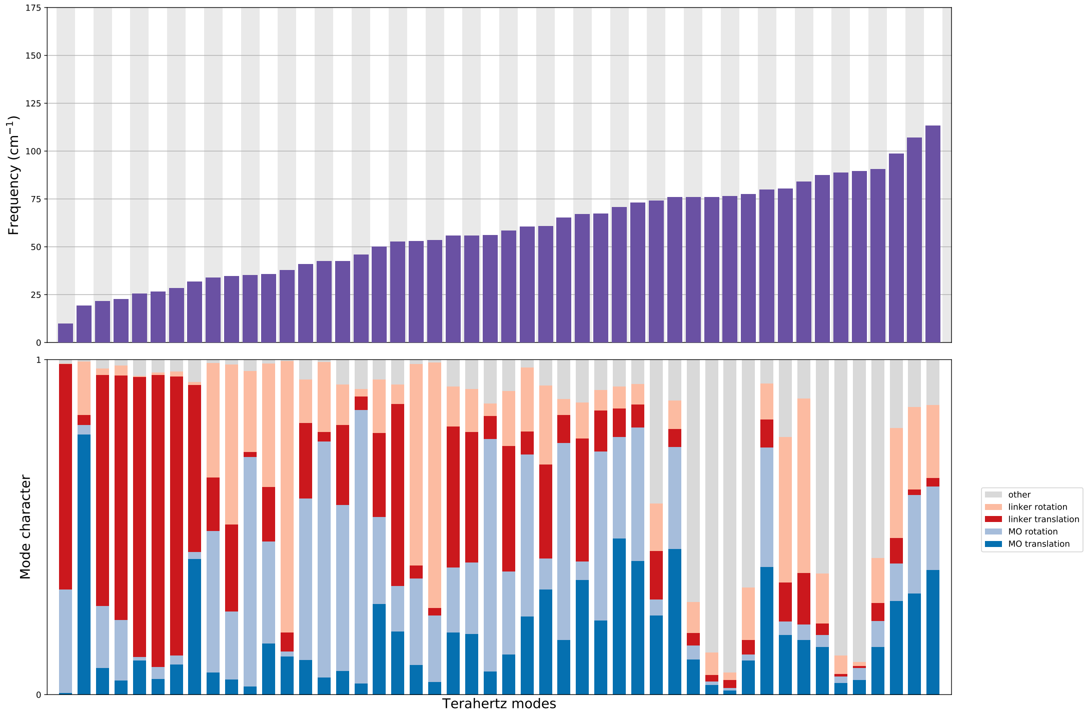

**Figure S51:** Mode frequency and character of the 48 phonon modes with the lowest frequency in the $2 \times 1 \times 1$ supercell of the lp phase of DUT-5(Al) containing a missing linker defect.

## Discussion

Focusing on the low-frequency phonon modes in the lp phase structures, it can be noticed that the mode character of these modes differs somehow between the ideal and defective structure. On the one hand, in the ideal supercell structure it is possible to identify exactly the same rigid unit modes found at the gamma point. Furthermore, the ideal $2 \times 1 \times 1$ supercell structure contains additional phonon modes with double degeneracy which have mode displacements in antiphase. On the other hand, the defective lp phase structures show phonon modes with similar frequencies than the ideal structure, but with slightly different mode character.

The presence of a defect lifts the degeneracy of phonon modes in antiphase and it changes the contribution of several building blocks to particular phonon modes. For example, defective structures no longer contain RUMs with almost 100 % displacement due to linker rotations (modes C). Instead this linker rotation is now combined with a significant portion of metal-oxide rotation, metal-oxide translation, and linker translation. In general, it becomes more difficult to observe a specific mode character in defective structures as the RUMs contain significant portions of all building blocks. By creating a more isolated defect in a $3 \times 1 \times 1$ supercell, it becomes again more easy to identify a specific mode character, such as rotation of the linker.

Just as in the case of defective lp phase structures, the defective cp phase structure of MIL-53(Al) contains mainly RUMs with significant contributions from all building blocks. However, whereas in the case of the defective lp phase structures the RUM frequencies were still similar to the ideal case, this is less so for the defective cp phase structures. The RUMs corresponding to the soft modes A and B yield a lower vibrational frequency in the defective structure, whereas the other RUMs show an increased vibrational frequency in the defective structure. The cause of these frequency changes can be found in the decreased unit cell volume of the defective structure (1612 Å$^3$ against 1683 Å$^3$ for the ideal supercell structure). In general, the increased repulsive forces due to neighboring building blocks will increase the RUM frequencies, except for modes A and B, which are entropically favored in dense structures.

It can be concluded that the presence of defects change the mode character of RUMs. When this defect has no consequences for the unit cell volume, the vibrational frequencies of the RUMs remain almost unaltered as is the case for lp phase structures. Defective structures in the cp phase do exhibit changes in RUM frequencies with respect to pristine structures as a result of changes in the unit cell volume.

## S11.2 Change in oxidation state

The influence of a change in oxidation state on the RUMs was investigated for the lp phase of MIL-53(V). Starting from the unit cell of MIL-53(V), the oxidation state of a single vanadium atom was changed from +III to +IV. As a consequence, one of the neighboring hydroxyl groups was deprotonated (see Figure S52). Identical to the case of the missing linker defects, the optimal geometry and corresponding Hessian of the defective structure is determined allowing to compare the normal modes with those of the pristine structure.

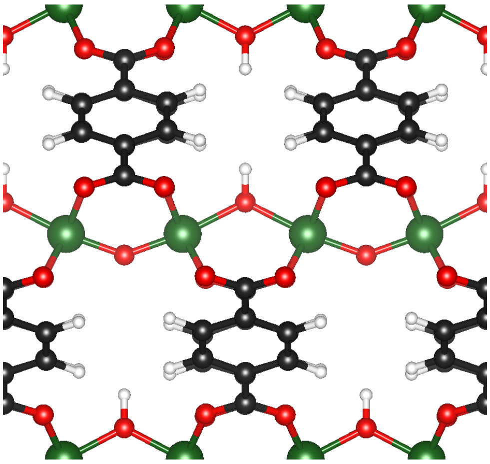

**Figure S52:** Visualization of the lp phase of MIL-53(V) with a changed oxidation state in a single vanadium atom.

The frequencies and character of the phonon modes with the lowest frequencies in the pristine and defective MIL-53(V) structure are presented in Figures S53 and S54, respectively. All RUMs identified in the pristine MIL-53(V) structure are also found in the defective structure with similar mode character. Also the RUM frequencies are almost identical except for the RUMs inducing linker rotations (modes C), which have consistently a slightly lower vibrational frequency in the defective structure. Therefore, it can be concluded that a change in oxidation state has almost no impact on the RUMs.

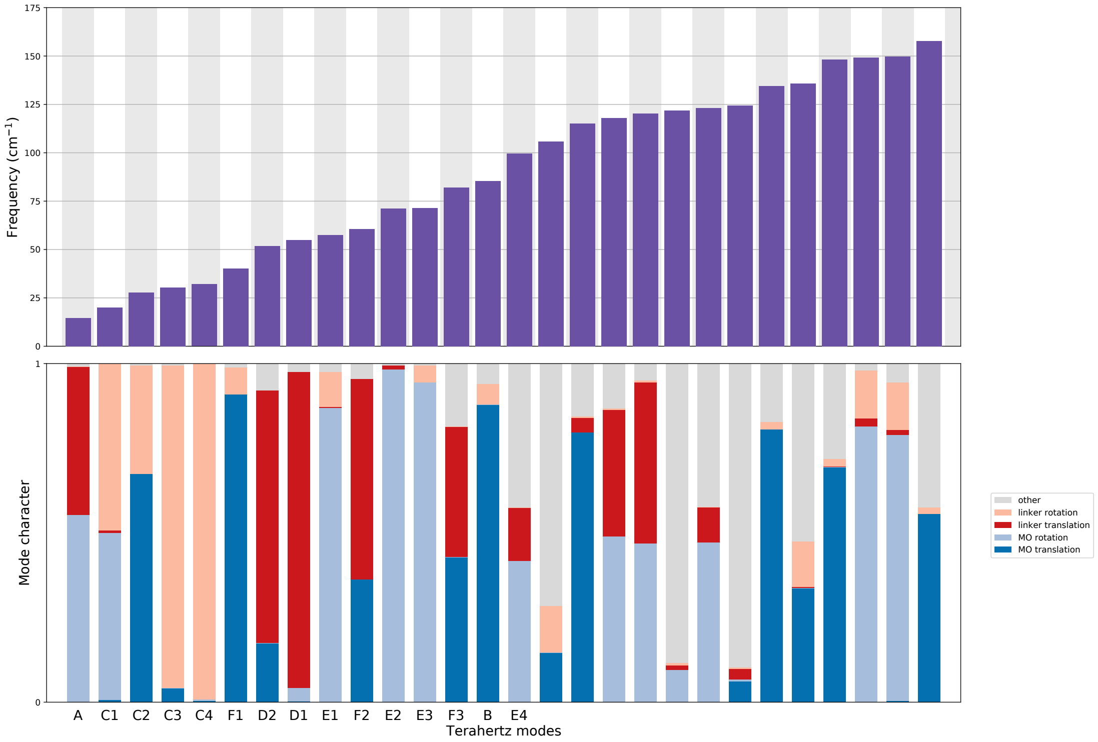

**Figure S53:** Mode frequency and character of the 28 phonon modes with the lowest frequency in the lp phase of MIL-53(V). The RUMs are indicated below.

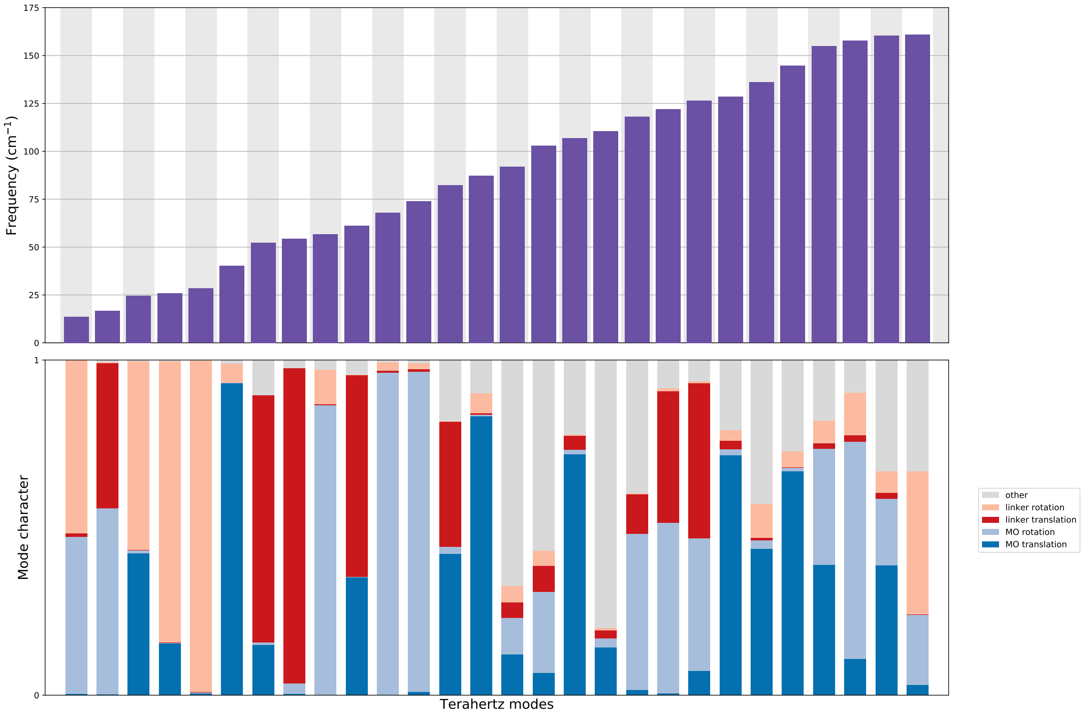

**Figure S54:** Mode frequency and character of the 28 phonon modes with the lowest frequency in the lp phase of MIL-53(V) with a changed oxidation state in a single vanadium atom.

### S11.3 Raman spectra of defective structures

In previous sections, the effect of defects on the character and frequencies of RUMs has been discussed. Here, the impact on spectroscopic fingerprints will be estimated through Raman spectroscopy. An experimental characterization of Raman fingerprints of defective structures is outside the scope of this theoretical study. However, our theoretical results can assist future experimental research.

Figures S55, S56, and S57 present the static DFT Raman spectra of the lp phase of MIL-53(Al), the cp phase of MIL-53(Al), and the lp phase of DUT-5(Al) with and without missing linker defect. The Raman spectra of the defective structures are very similar to the ones of the pristine structures. Several Raman bands are slightly shifted, but no new peaks can be observed. Especially the cp phase of MIL-53(Al) shows a clear shift of one of the Raman bands due to a RUM inducing linker rotations. This shift was already predicted from the above RUM analysis (see Section S11.1). Interpreting the results of our small periodic model in the light of large realistic samples, it can be expected that Raman spectra of defective structures exhibit broadened bands due to these frequency shifts.

Above, the focus was on Raman features due to missing linker defects. When the oxidation state of a metal atom is changed, it can be expected that no clear differences in the Raman spectra occur. At least not in the low-frequency spectrum, based on the very small differences that were observed in the RUM analysis (see section S11.2). Other types of defects, such as missing metal nodes, may have a larger impact on the Raman spectrum, but were not considered in this study.

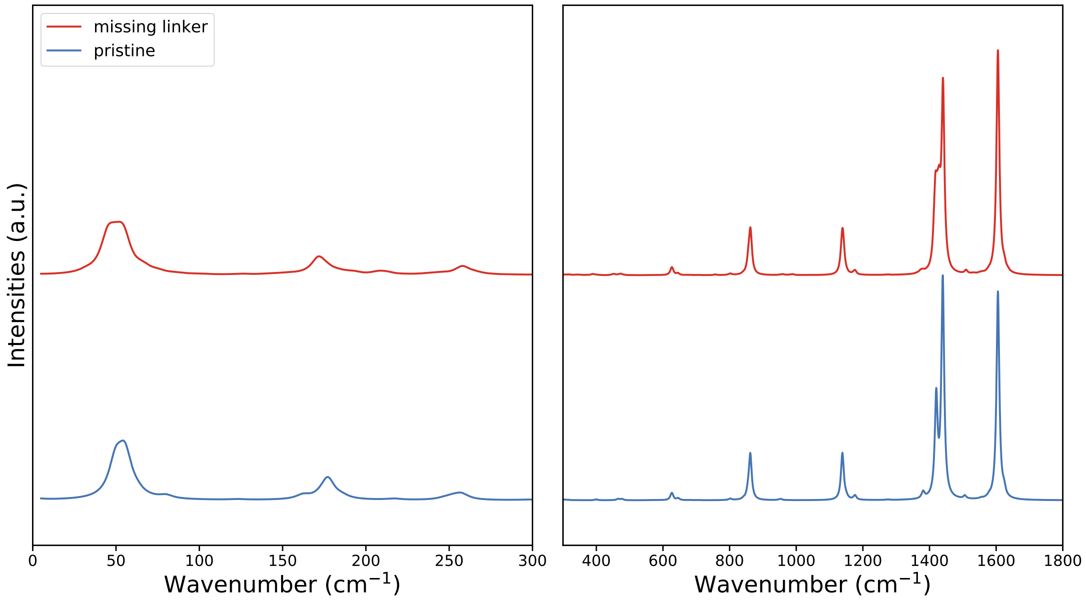

**Figure S55:** Static DFT Raman spectra of the lp phase of MIL-53(Al) with (red) and without (blue) missing linker defect.

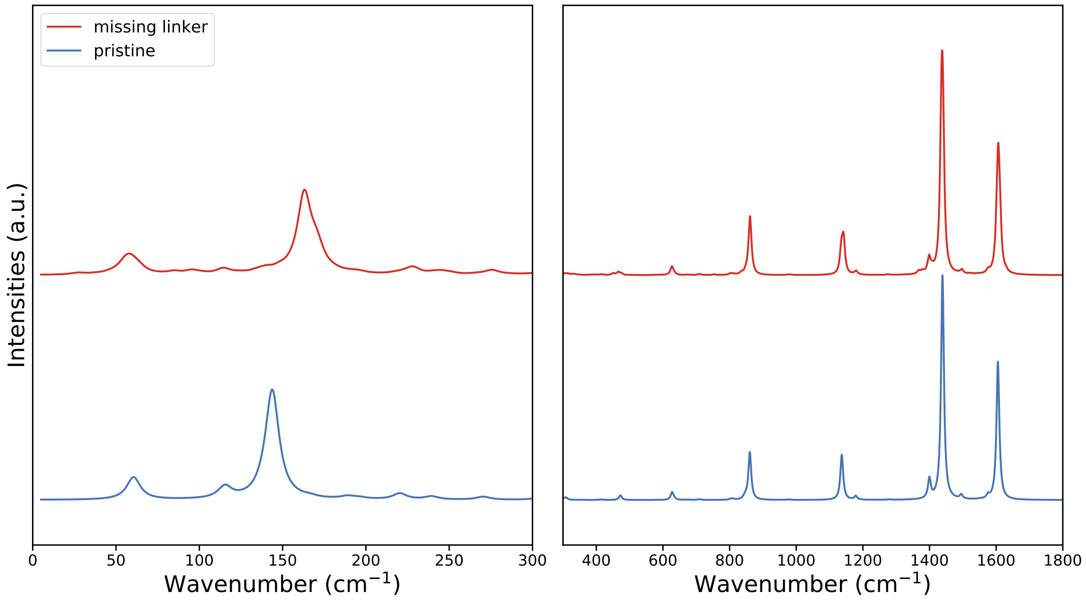

**Figure S56:** Static DFT Raman spectra of the cp phase of MIL-53(Al) with (red) and without (blue) missing linker defect.

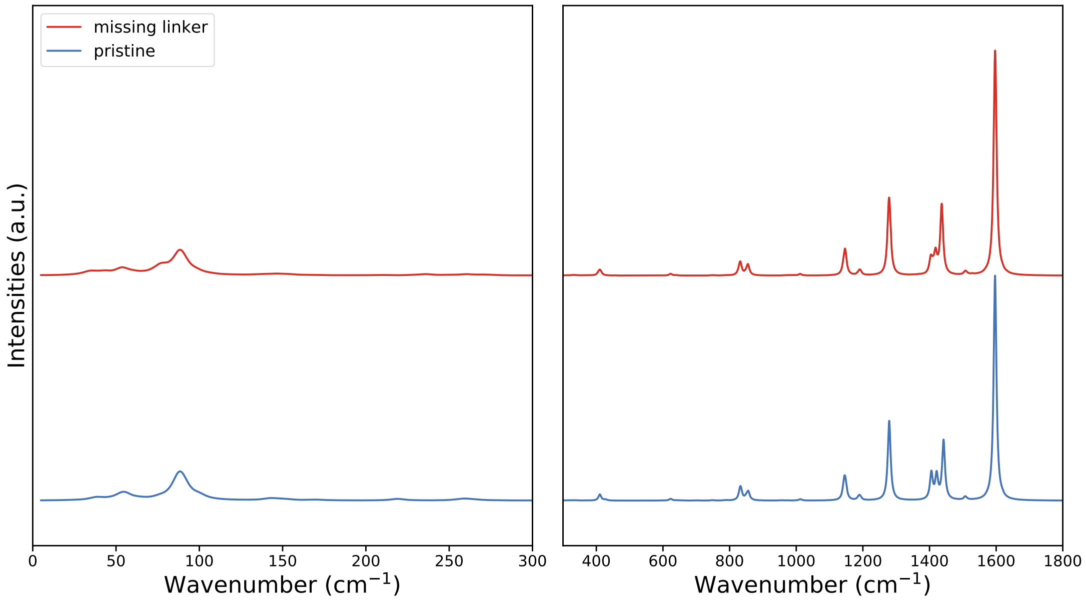

**Figure S57:** Static DFT Raman spectra of the lp phase of DUT-5(Al) with (red) and without (blue) missing linker defect.

## S12 Effect of temperature on phonon modes

The rigid unit modes discussed in this work are computed via static DFT calculations, which corresponds to the situation at 0 K. However, lattice dynamics can be influenced by temperature. To estimate the impact of temperature on the phonon modes, AIMD simulations have been performed on a subset of the MIL-53 analogs and their terahertz spectrum is analyzed via the Raman spectrum. The calculations were performed with the same computational settings discussed in Section S4.1. The lp and cp phases of MIL-53(Al) are investigated to compare the effect of temperature on phonon modes in both phases (see Figures S58 and S59). Furthermore, the lp phase of DUT-5(Al) is studied to analyse the change in response to temperature of the phonon modes after linker substitution (see Figure S60). Finally, also MIL-53(Al)-F is taken into consideration to estimate the effect of the compensating anion (see Figure S61). First of all, there is a good correspondence between AIMD Raman spectra at 100 K and static DFT Raman spectra for all structures. At higher temperatures, a different temperature response is noticed for the cp and the lp phases. The Raman spectrum of the cp phase of MIL-53(Al) does not change significantly as a function of temperature. Only a broadening of the Raman bands is observed. In contrast, the lowest Raman bands for the lp phase structures, due to phonon modes inducing linker rotations, exhibit a shift to lower frequencies. This may indicate that the lp phase becomes even more entropically favored at higher temperatures than initially predicted by static DFT.

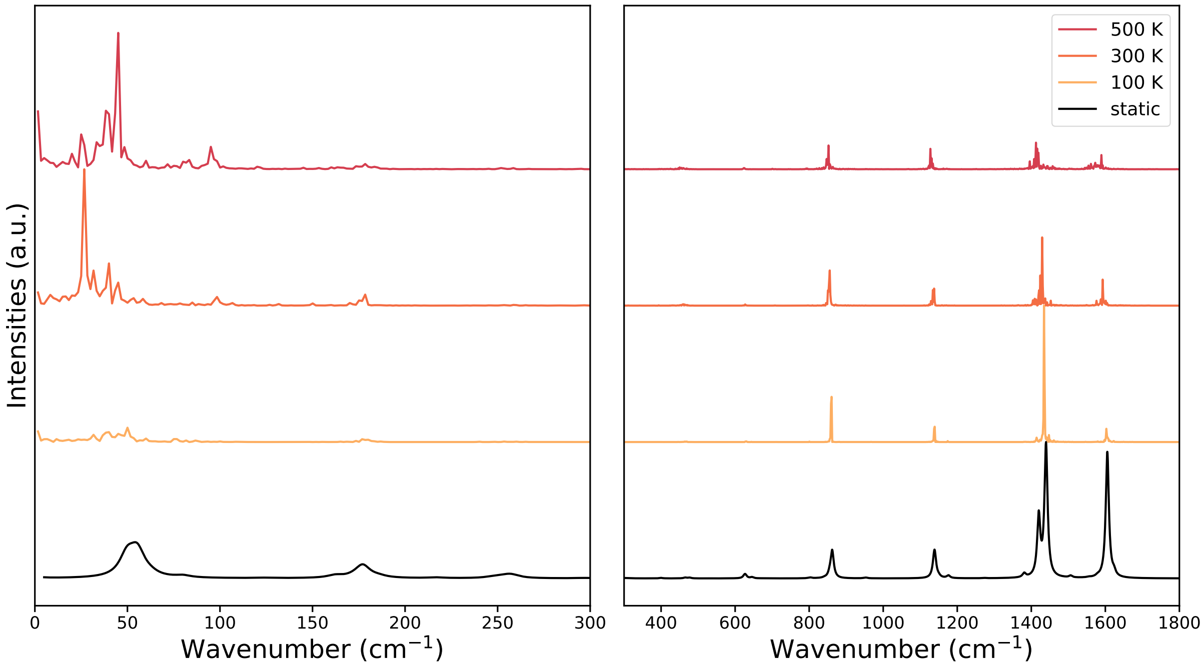

**Figure S58:** AIMD Raman spectra of the lp phase of MIL-53(Al) at 100 K (yellow), 300 K (orange), and 500 K (red) compared with the static DFT Raman spectrum (black).

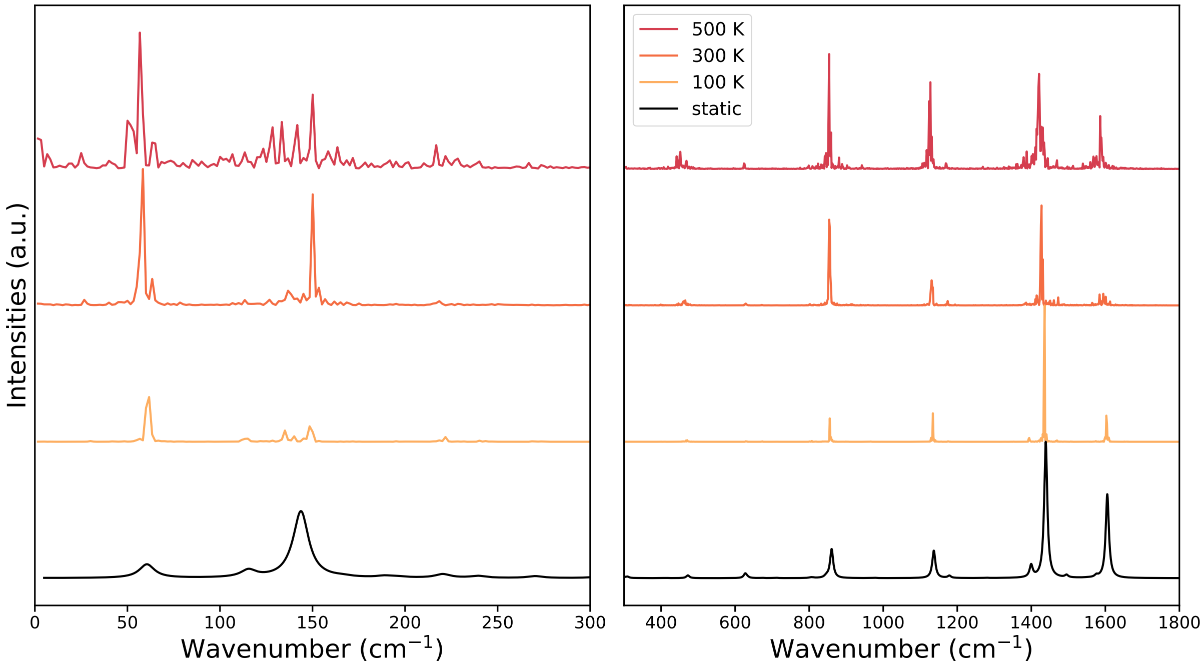

**Figure S59:** AIMD Raman spectra of the cp phase of MIL-53(Al) at 100 K (yellow), 300 K (orange), and 500 K (red) compared with the static DFT Raman spectrum (black).

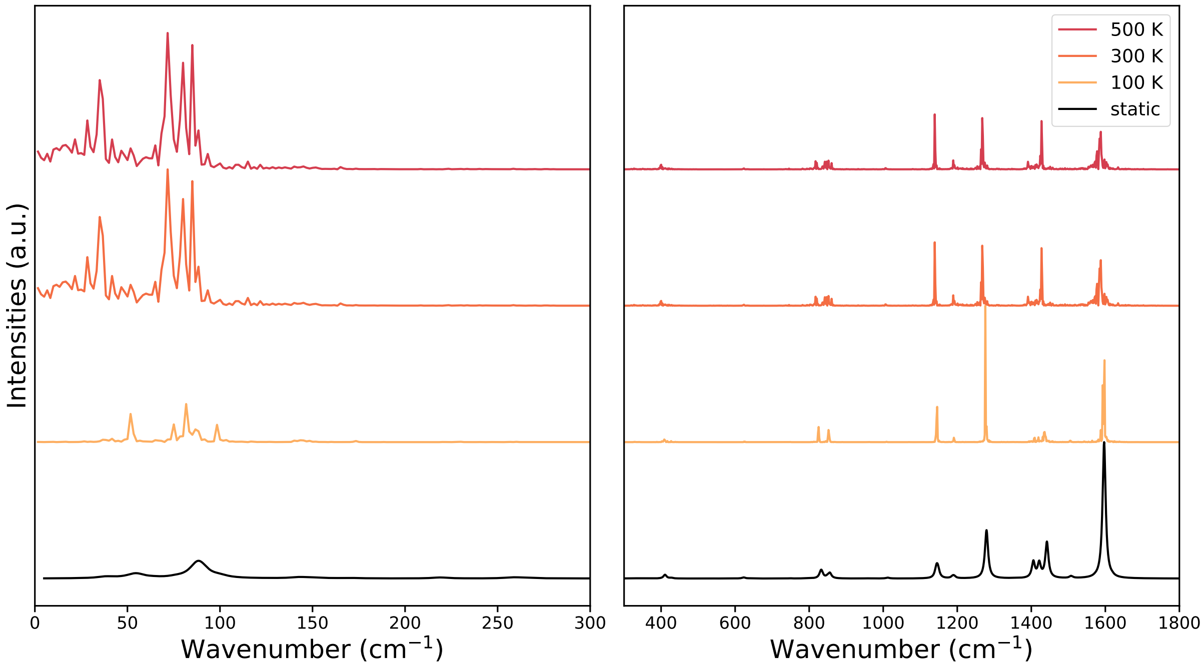

**Figure S60:** AIMD Raman spectra of the lp phase of DUT-5(Al) at 100 K (yellow), 300 K (orange), and 500 K (red) compared with the static DFT Raman spectrum (black).

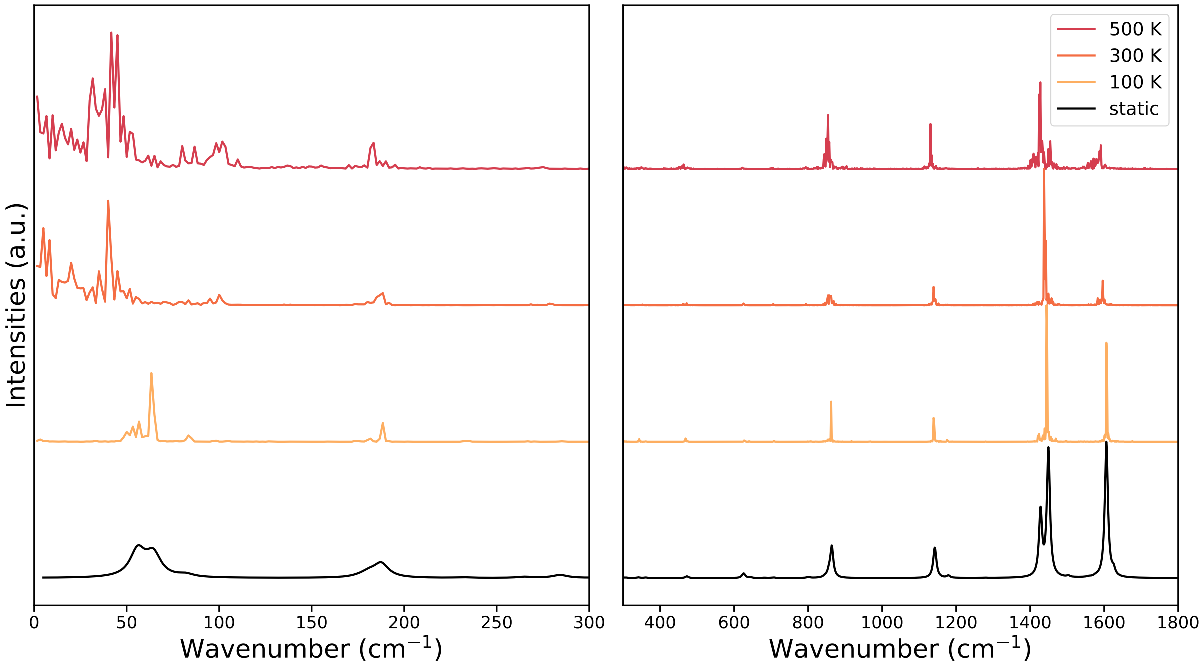

**Figure S61:** AIMD Raman spectra of the lp phase of MIL-53(Al)-F at 100 K (yellow), 300 K (orange), and 500 K (red) compared with the static DFT Raman spectrum (black).

# References

[1] T. D. Kühne, M. Iannuzzi, M. Del Ben, V. V. Rybkin, P. Seewald, F. Stein, T. Laino, R. Z. Khaliullin, O. Schütt, F. Schiffmann, D. Golze, J. Wilhelm, S. Chulkov, M. H. Bani-Hashemian, V. Weber, U. Borštnik, M. Taillefumier, A. S. Jakobovits, A. Lazzaro, H. Pabst, T. Müller, R. Schade, M. Guidon, S. Andermatt, N. Holmberg, G. K. Schenter, A. Hehn, A. Bussy, F. Belleflamme, G. Tabacchi, A. Glöß, M. Lass, I. Bethune, C. J. Mundy, C. Plessl, M. Watkins, J. VandeVondele, M. Krack, and J. Hutter, "CP2K: An electronic structure and molecular dynamics software package - Quickstep: Efficient and accurate electronic structure calculations,"

[2] J. P. Perdew, K. Burke, and M. Ernzerhof, "Generalized gradient approximation made simple," *Phys. Rev. Lett.*, vol. 77, no. 18, p. 3865, 1996.

[3] S. Grimme, "Semiempirical GGA-type density functional constructed with a long-range dispersion correction," *J. Comput. Chem.*, vol. 27, no. 15, pp. 1787–1799, 2006.

[4] S. Grimme, S. Ehrlich, and L. Goerigk, "Effect of the damping function in dispersion corrected density functional theory," *J. Comput. Chem.*, vol. 32, no. 7, pp. 1456–1465, 2011.

[5] G. Lippert, J. Hutter, and M. Parrinello, "A hybrid Gaussian and plane wave density functional scheme," *Mol. Phys.*, vol. 92, no. 3, pp. 477–488, 1997.

[6] J. VandeVondele and J. Hutter, "Gaussian basis sets for accurate calculations on molecular systems in gas and condensed phases," *J. Chem. Phys.*, vol. 127, no. 11, p. 114105, 2007.

[7] S. Goedecker, M. Teter, and J. Hutter, "Separable dual-space Gaussian pseudopotentials," *Phys. Rev. B*, vol. 54, no. 3, p. 1703, 1996.

[8] G. J. Martyna, M. L. Klein, and M. Tuckerman, "Nosé–Hoover chains: The canonical ensemble via continuous dynamics," *J. Chem. Phys.*, vol. 97, no. 4, pp. 2635–2643, 1992.

[9] G. J. Martyna, D. J. Tobias, and M. L. Klein, "Constant pressure molecular dynamics algorithms," *J. Chem. Phys.*, vol. 101, no. 5, pp. 4177–4189, 1994.

[10] M. Thomas, M. Brehm, R. Fligg, P. Vöhringer, and B. Kirchner, "Computing vibrational spectra from ab initio molecular dynamics," *Phys. Chem. Chem. Phys.*, vol. 15, no. 18, pp. 6608–6622, 2013.